Engineering Geology 346 (2025) 107907

Contents lists available at ScienceDirect

Engineering Geology

journal homepage: www.elsevier.com/locate/enggeo

A multi-method approach in the physical and mechanical assessment of lava rocks with distinct microstructure

Maria Luísa Pereira [a,b,*], Lucia Pappalardo [c], Gianmarco Buono [c], Nora Cueto [d,e], Carmen Vázquez-Calvo [e], Rafael Fort [e], Matilde Costa e Silva [f], Isabel Fernandes [g], Vittorio Zanon [a], Paulo Amaral [h]

[a] Instituto de Investigação em Vulcanologia e Avaliação de Riscos (IVAR), Universidade dos Açores, Rua Mãe de Deus, Ponta Delgada 9500-123, Portugal
[b] Faculdade de Ciências e Tecnologia, Universidade dos Açores, Rua Mãe de Deus, Ponta Delgada 9500-123, Portugal
[c] Istituto Nazionale di Geofisica e Vulcanologia, Osservatorio Vesuviano, Via Diocleziano, 328, 80124 Naples, Italy
[d] Departamento de Ciencias de la Tierra y del Medio Ambiente, Universidad de Alicante, C. San Vicente del Raspeig s/n, 03690 San Vicente del Raspeig, Alicante, Spain
[e] Instituto de Geociencias IGEO (CSIC - UCM), c/Doctor Severo Ochoa, 7, 28040 Madrid, Spain
[f] CERENA, DECivil, Técnico Lisboa, Universidade de Lisboa, Avenida Rovisco Pais 1, 1049-001, Lisbon, Portugal
[g] Instituto Dom Luiz (IDL), Faculdade de Ciências, Universidade de Lisboa, Campo Grande, 1749-016 Lisbon, Portugal
[h] Laboratório Regional de Engenharia Civil (LREC), Edifício LREC, Rua de S. Gonçalo, 9500-343 Ponta Delgada, Portugal

ARTICLE INFO

Keywords:
Petrophysical and mechanical properties
Heterogeneity
Volcanic rocks
Digital rock physics
Pore network model
Mercury porosimeter

ABSTRACT

Volcanic rocks are common geological-geotechnical units with several heterogeneities. Their microstructural influence on deformation remains unexplored in engineering contexts. This study presents a comprehensive assessment of lava rocks ranging from basalts to trachytes, comprising massive and vesicular textures, varying degrees of fracturing and distinct pore size distributions. A multi-method approach combining X-ray microtomography, thin section analysis, and mercury intrusion porosimetry allowed to characterise the pore space and crystals at distinct scales and define fluid transport mechanisms. Digital rock physics allowed for determining absolute permeability and porosity and developing novel pore network models. Mechanical tests during time-resolved 3D X-ray imaging allowed for fracture development visualisation on varied lavas. Additional physical and mechanical properties were determined following international standards.

Results show that porosity (4 %-29 %) is primarily influenced by pore size and connectivity rather than vesicle shape or orientation. Macrovesicles (> 15 μm) are sub-spherical, while low sphericity indicates vesicle coalescence and fractures, which reduce rock strength and stiffness more than the feldspar content. Vesicular specimens (effective porosities above 10 %) have a permeability controlled by the vesicle size, while the number of microcracks and porosity define permeability in both massive and fractured lavas.

This study highlights the importance of microstructural assessment as a foundation for geological and geotechnical investigations, enabling informed material selection and building conservation strategies. The adopted analysis strategy, which combines techniques often used separately, has proven effective and is suggested for extending to the study of other complex materials.

1. Introduction

The complex origin of volcanic rocks manifests in their varied microstructure (Rust and Cashman, 2011; Sparks et al., 2019), leading to unpredictable deformation and engineering properties (e.g., Pappalardo and Mineo, 2017). Permeability and mechanical properties are known to depend on porosity, size, shape, and orientation of voids and

Abbreviations: μCT, X-ray microtomography; asl, above sea level; B.P., before present; CN, coordination number; COV, coefficient of variation; FMW, F for felsic, M for mafic, and W for weathering degree; ISRM, International Society for Rock Mechanics and Rock Engineering; MIP, mercury intrusion porosimeter; PSD, pore size distribution; UCS, unconfined compressive strength or uniaxial compressive strength.

* Corresponding author.
E-mail addresses: maria.lm.pereira@uac.pt (M.L. Pereira), lucia.pappalardo@ingv.it (L. Pappalardo), gianmarco.buono@ingv.it (G. Buono), nora.cueto@ua.es (N. Cueto), carmenvazquez@geo.ucm.es (C. Vázquez-Calvo), rafael.fort@csic.es (R. Fort), matilde.horta@tecnico.ulisboa.pt (M. Costa e Silva), mifernandes@fc.ul.pt (I. Fernandes), vittorio.vz.zanon@azores.gov.pt (V. Zanon), paulo.ap.amaral@azores.gov.pt (P. Amaral).

https://doi.org/10.1016/j.enggeo.2025.107907
Received 2 October 2024; Received in revised form 27 December 2024; Accepted 8 January 2025
Available online 10 January 2025

Nomenclature

Variables

ρ	dry bulk density
ρ_{ISRM}	bulk density determined by ISRM (2007) method using saturation and buoyancy techniques on irregular lumps
$\rho_{adp.ISRM}$	dry bulk density determined by an adaptation of ISRM (2007) method using saturation and buoyancy techniques on prisms of smaller dimension
n	porosity
$n_{T\_2D;\ PC}$	total porosity determined on a thin section by point counting (PC)
$n_{T\_2D;\ IA}$	total porosity determined on a thin section by image analysis (IA)
$n_{T\_\mu CT}$	total porosity determined from μCT images
n_{eff_ISRM}	effective porosity determined by ISRM (2007) method for irregular lumps
$n_{eff\_adp.ISRM}$	effective porosity determined by an adaptation of ISRM (2007) method using prisms of smaller dimension
$n_{eff\_\mu CT}$	effective porosity from μCT images
$n_{isol\_\mu CT}$	isolated porosity from μCT images
n_{eff_Hg}	effective porosity determined by mercury porosimeter
k	absolute permeability
r	mean pore radius
ϕ	- orientation of an object defined between the z-axis and the radial line, within 0 to 90 degrees, and computed with the inertia moments. Also known as polar angle or inclination angle.
E_{avg}	average Young's modulus
E_{tg}	tangent Young's modulus
E_{sec}	secant Young's modulus

phenocrysts (Bubeck et al., 2017; Griffiths et al., 2017; Colombier et al., 2017a; Heap et al., 2014a; Heap et al., 2018; Heap et al., 2022; Pappalardo et al., 2017, 2024; Vairé et al., 2024), crystal content (Heap and Wadsworth, 2016; Zorn et al., 2018), and alteration (Jamtveit et al., 2011; Vieira et al. 2021; Liu et al., 2023). Nonetheless, the interplay between microcracks, vesicles, and crystals and their implications for the deformation of volcanic rocks (Heap et al., 2014b; Zhu et al., 2016; Heap and Wadsworth, 2016; Heap et al., 2020a) and durability of diverse rock materials (Török and Přikryl, 2010; Hamdi and Lafhaj, 2013; Barone et al., 2015) remains unclear due to their complexity. Additional microstructural data could offer deeper insights, as well as provide key input values for geomechanical classifications (Bieniawski, 1989; González de Vallejo and Ferrer, 2011; Miranda et al., 2015) and numerical models of rock failure to predict engineering properties and better comprehend fracture mechanics (e.g., Bubeck et al., 2017; Griffiths et al., 2017; Reinoso et al., 2019).

Various techniques have been used to assess the microstructure of volcanic rocks, including digital rock physics, which combines X-ray microtomography (μCT) with 3D image analysis and advanced numerical simulations (Higgins, 2000, 2006; Baker et al., 2012; Cnudde and Boone, 2013). μCT is non-destructive and allows for direct visualisation and quantification of the 3D internal structure of rock samples, under submicron resolutions, requiring little to no sample preparation (e.g., Landis and Keane, 2010; Pappalardo et al., 2018). For volcanic rocks, 3D imaging of the internal structure of the solidified lavas informs about magma emplacement history and direction of flow (Walker, 1987; Song et al., 2001; Jamtveit et al., 2011; Polacci et al., 2018; Couves et al., 2016; Bubeck et al., 2017; Becker et al., 2019; Heap et al., 2020a; Liu et al., 2023; Vairé et al., 2024). Applications of μCT have been leveraged to four dimensions by tracking the 3D evolution of a structure over time, which provides a dynamic view of changes as they occur (e.g., Dvorkin et al., 2011; Noiriel and Renard, 2022) and allows for the analysis of various processes, such as monitoring how a structure responds to mechanical loading (compression and tension) (e.g., McBeck et al., 2020), investigating thermal effects on material properties and behaviours (e.g., Lintao et al., 2017; Fan et al., 2018; Polacci et al., 2018), and visualising fluid dynamics within porous networks (e.g., Noiriel and Renard, 2022). Therefore, μCT can be combined with conventional 2D imaging (e.g., Heap et al., 2014b; Zhu et al., 2016) and laboratory methods (Heap and Violay, 2021; Lavallée and Kendrick, 2021) to comprehensively define the microstructure and properties of complex geomaterials, such as volcanic rocks.

Lava rocks are a widespread geological formation and constitutes the main component of volcanic islands, frequently used as resources and intercepted in most construction sites. In S. Miguel Island (the Azores, Portugal), lava rocks are heterogenous but competent geological-geotechnical units susceptible to seismic and volcanic hazards, together with the extreme meteorological events (Malheiro, 2006; Malheiro and Nunes, 2007). Despite exploited for several engineering applications, like construction and building materials purposes, few studies focus on their physical and mechanical properties (Loaiza et al., 2012; Moreira and Wallenstein, 2012), while their microstructure remains unexplored.

A multi-method study from a meso- to microscale was performed on lava rocks representative of the stratigraphy and subsurface geology of two volcanoes of S. Miguel Island – Fogo and Sete Cidades, constituting the first thorough microstructural research on these materials. The applied strategy involved the investigation of content, size, and shape of vesicles and crystals using 3D digital rock physics combined with 2D textural analysis on thin sections. The suggested methods of ISRM (International Society for Rock Mechanics and Rock Engineering) and mercury intrusion porosimeter (MIP) were both applied to quantify physical properties (effective porosity and bulk density). The pore space characterisation (pore size distribution, mean pore size, effective porosity) was integrated with the calculation of absolute permeability values and with pore network models. The behaviour of lavas under unconfined compressive conditions was assessed using μCT, and their strength was further quantified on larger specimens tested according to ISRM's suggested methods.

The merged data enhances the scarce knowledge on the petrophysical and mechanical properties of lava rocks from the Azores. While this study focuses on local materials, the integration of conventional and cutting-edge techniques effectively characterises varied lava rocks and can be applied to other heterogeneous materials. The findings highlight the influence of both pores and phenocrysts on mechanical and hydraulic properties and crack development, underscoring the importance of microstructural assessment as a critical first step in selecting rock materials for engineering purposes. Considering microstructural parameters of voids and crystals could also improve classification systems and testing protocols, particularly for building materials susceptible to long-term deterioration and natural hazards.

2. Materials and methods

2.1. Materials

2.1.1. Geological setting

S. Miguel Island, located in the middle of the Atlantic Ocean, is volcanically and seismically active, with a history of destructive earthquakes, volcanic unrest episodes, and numerous eruptions occurring in the last 5 ka (Silva et al., 2015; Gaspar et al., 2015). S. Miguel exhibits an elongated east-west shape (Fig. 1), formed by the products erupted by Sete Cidades, Fogo or Água de Pau, Furnas and Nordeste polygenetic volcanoes, interconnected by fissure zones (Moore, 1991a). The activity of polygenetic volcanoes occurred during different phases of magmatism, producing early basaltic eruptions followed by later explosive trachytic magma emissions (Zanon, 2015; Larrea et al., 2018). The

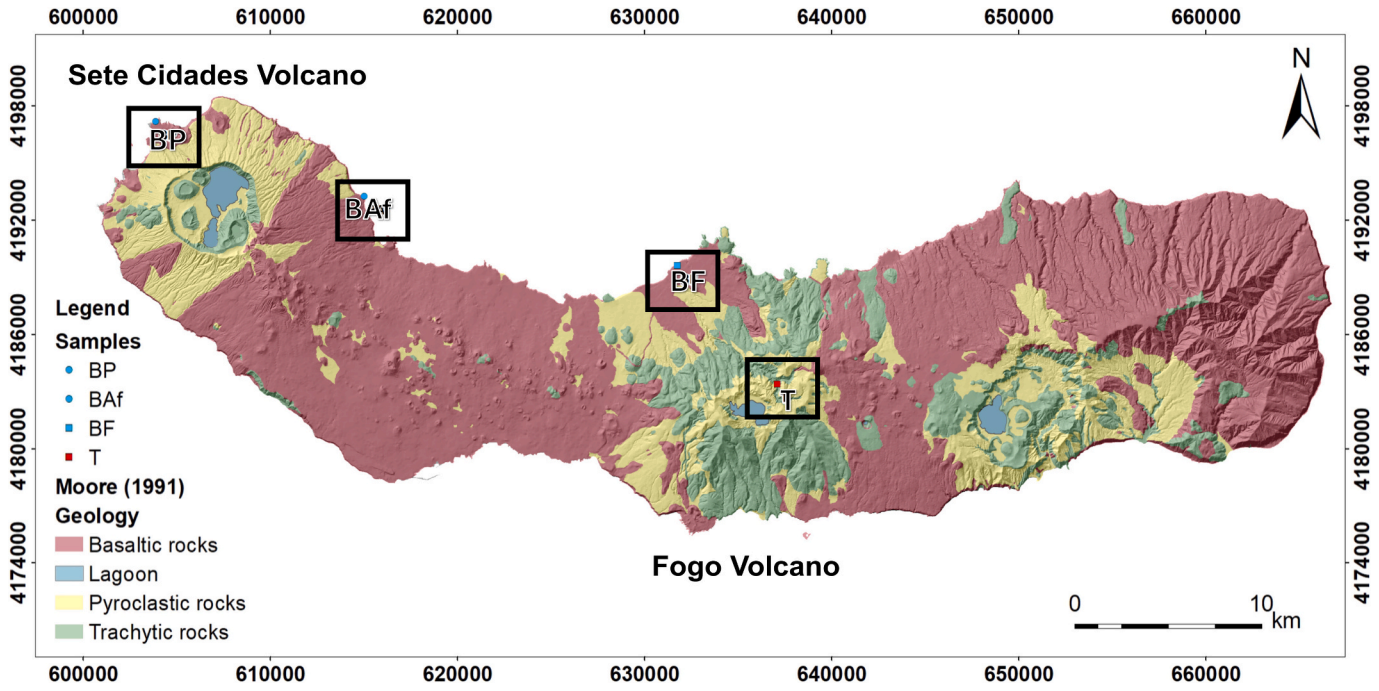

Fig. 1. Simplified geological map of the sampling area (adapted from Moore, 1991b).

nearby Terceira Rift influences the tectonic structures of the island, with a NW-SE and WNW-ESE trend (Searle, 1980; Miranda et al., 2015).

The Fogo and Sete Cidades volcanoes were chosen for lava block collection (Fig. 1). Fogo Volcano (> 200,000 years), occupies 150 km^2 at the centre of the island, rises 947 m above sea level (asl) and features a 3.2 km diameter caldera hosting a lake at its summit (Wallenstein et al., 2015). Fogo volcano has an active high-temperature geothermal field in its northern flank and the last unrest period, marked by seismic activity and ground deformation, was attributed to magmatic intrusion, hydrothermal fluid ascension, or both (Trota, 2009; Silva et al., 2015; Okada et al., 2015; D'Araújo et al., 2022a, 2022b). The base of the Sete Cidades volcanic system is older than 210,000 years and its subaerial products cover about 110 km^2 on S. Miguel's western end, rising 845 m asl. The volcano comprises a 5 km diameter summit caldera (Queiroz et al., 2015).

2.1.2. Sampling and sample preparation

Basalts (*s.l.*) and trachytes are the main lava rocks in S. Miguel, widely spread throughout the island and composing the general stratigraphy and subsurface geology of S. Miguel's volcanoes (e.g., Muecke et al., 1974; GeothermEx, 2008; Pereira et al., 2022). Both lithologies are described as "hard" geotechnical units (Malheiro and Nunes, 2007). A total of 10 basaltic to trachytic lava blocks (maximum ~20 cm × 20 cm × 20 cm), representative of Fogo and Sete Cidades volcanic systems, were sampled from accessible outcrops to facilitate the handling of the blocks (Fig. 1).

Basalts were collected on the coast of Mosteiros (BP) and Santo António villages (BAf) in available lava flow cores produced in flank eruptions of Sete Cidades volcano. As regards Fogo, chemically intermediate lava blocks were collected from a lava flow at Ribeirinha village (BF). Massive and vesicular blocks were obtained to quantify their physical and mechanical differences. Several quarries are displayed near to Ribeirinha village, where similar rocks are explored for construction and building materials purposes, making an important geological resource from the island. Trachytes (T) were collected at Vale das Lombadas and are representative of materials present in domes and flows of the island and composing the shallower levels of the geothermal system from Fogo volcano (GeothermEx, 2008).

The specimens are obtained from numbered blocks (e.g., BP37 and BP38), with earlier numbers corresponding to blocks not covered by this research. Blocks were cored and cut into specimens according to standard instructions for the different tests. Five basaltic (BP37, BP38, BAf14, BAf16, BAf18), three intermediate (BF3, BF13, BF15) and two trachytic (T29, T31) were selected for this investigation (Fig. 2).

2.2. Methodology

2.2.1. Petrography, geochemistry, texture and microstructure

A petrographic study was conducted on the 10 lava samples using polished thin sections and optical microscopes (Leica DM750O polarising microscope equipped with a Leica ICC50HD camera). Voids and crystals were quantified by point counting (Nikon ECLIPSE E200 and PetrogLite software). Microstructure was further investigated using a benchtop scanning electron microscope (SEM; Hitachi T4000 Plus), where full high-resolution 2D scans (15 kV; X100 optical magnification; 2.74 to 2.86 μm resolution; backscattered mode - BSE – Table SI.1; Supplementary Information - SI) of the polished thin sections were obtained. Whole-rock chemistry (major elements fusion; ICP-OES) was performed on Actlabs Ltd. (Canada) and the geochemical data was classified with the GCDkit package from R 4.1.3.

Zeiss Xradia Versa-410 μCT equipment of the Istituto Nazionale di Geofisica e Vulcanologia – Osservatorio Vesuviano (INGV-OV; Italy) was employed to scan prisms of ~11.5 mm × 16/20 mm of all 10 samples in 3D (Fig. SI.1; Table SI.1). X-ray imaging was performed in absorption mode acquiring 1601 2D radiographs (projections) over a 360° rotation with 100 to 120 kV voltage, 10 W power, variable exposure time (0.7 to 1.2 s). Appropriate source filters were used to minimise beam hardening. An optical magnification of 0.4× was used, resulting in a nominal voxel size between 14.68 μm and 15.37 μm (Table SI.1). The voxel sizes result from trade-off between resolution to resolve the pore space, while guaranteeing sample representativeness and acceptable scan times. The acquired projections were then reconstructed through a filtered back-projection algorithm using XRMReconstructor software by ZEISS, providing 3D greyscale images of the internal microstructure of the samples (Fig. 2), proportional to the X-ray attenuation coefficient of the rock phases, which is a function of their density and composition.

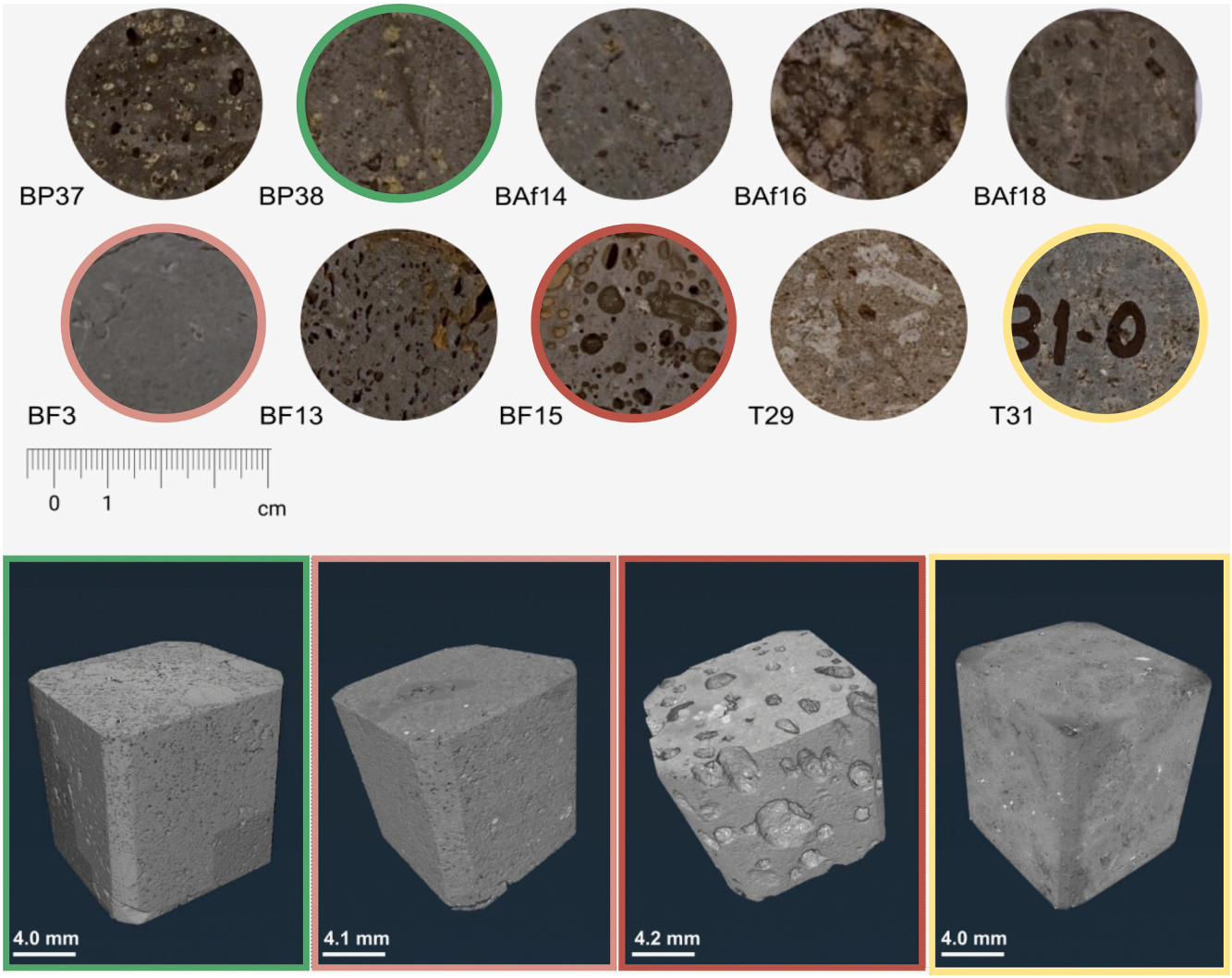

Fig. 2. Texture of the hand specimens per sample and 3D X-ray microtomography image of an alkali basalt (BP38; green), a massive intermediate lava rock (BF3; pink), a vesicular intermediate rock (BF15; red), and a trachyte (T31; yellow). (For interpretation of the references to colour in this figure legend, the reader is referred to the web version of this article.)

The 10 specimens used in the μCT were further analysed for connected porosity (n_{eff_Hg}), mean porous radius (r) and pore size distribution (PSD) measurements by mercury intrusion porosimeter (MIP) through a Micromeritics Auto Pore IV 9520, a 60,000 psi (414 MPa) mercury porosimeter covering the pore radius range from approximately 0.0015 to 180 μm. Penetrometers designed for solids were used. Specifically, penetrometers of 5 cc sample volume, maximum measurable volume of 0.366 cc and total stem volume of 0.392 cc. Samples were dried at 70 °C until constant weight before characterisation.

2.2.2. Physical tests

The bulk density (ρ) and porosity (n) measurements on the specimens of all the 10 samples were acquired using saturation and buoyancy techniques described by the ISRM method (ISRM, 2007; ρ_{ISRM}; n_{eff_ISRM}). Both quick water immersion and paraffin immersion (Crawford, 2013) were further performed in an electronic densimeter (MD-2005; $\rho_{adp.ISRM}$; $n_{eff\_adp.ISRM}$). The ISRM (2007) method comprised the saturation under vacuum under 800 Pa in a vacuum chamber, which was also performed on the prismatic specimens. One prism per sample was tested in the μCT equipment. These have smaller dimensions than the irregular lumps used in the saturation and buoyancy techniques (ISRM, 2007), which have 10 times the maximum grain size and a weight ≥ 50 g.

2.2.3. Mechanical tests

Unconfined compressive strength (UCS) experiments combined with μCT imaging were performed on four representative cylinder specimens (i.e., BAf14, BF3, BF13, and T31 samples – Fig. SI.1) with a ~ 7.5 mm diameter and a length-diameter ratio of approximately 1.9 (Table SI.1). The test was conducted using a loading rate of 0.03 mm/min and a Deben in-situ load cell stage (CT5000H250), with a maximum load capacity of 5210 N, incorporated into the Zeiss equipment of the INGV-OV. Pre and post-test 3D scans were obtained, and Young's modulus (or elastic modulus; E) was calculated based on stress-strain curves derived from the plate displacement. X-ray imaging of the cylinders was performed collecting 801 projections over a total angular scan of 180° (plus fan angle) with a scan time between 2.75 and 3.5 s per projection at 120 kV and 10 W and using an optical magnification of 0.4× to obtain 3D images with a voxel size of 15 μm (Table SI.1).

Additional compressive strength tests were carried out using specimens with 45 mm diameter and a length: diameter ratio of 2 (intact rock scale; ASTM D7012–23, 2023) and following ISRM (2007) suggestions. A servo-controlled press FORM + TEST D-88499, with a maximum load capacity of 1000 kN, using a 0.5 MPa/s stress rate and a peak sensitivity of 95 % was used. For strain measurements, four strain gauges (PFL-30-11-5LJC-F; 30 mm; 2.09 ± 1 % sensitivity; 118.5 ± 0.5 Ω resistance) were glued into the specimen, separated by 90° each. At the beginning of

each test, three cycles of load and unload in the elastic regime were performed to ensure a more accurate stress-strain relation.

Distinct elastic modulus (average - E_{avg}, tangent - E_{tg}, and secant- E_{sec}) were determined for the two types of UCS tests, as their results have been found to vary considerably (Małkowski et al., 2018). For the tangent modulus, 50 % of the ultimate strength is considered, for the secant modulus, the slope is determined between the origin and 50 % of the stress-strain curve, while the average modulus is based on the straight-line section of the stress-strain curve, following ISRM (2007).

2.2.4. Data analysis and simulations

3D μCT and 2D SEM scanned images were analysed using PerGeos software. Image filtering and segmentation by manually thresholding the grey level histogram allowed to segment pores. Phenocrysts exhibit similar X-ray attenuation values with the groundmass which difficult their segmentation, so a machine learning-based texture-supervised classification was applied. Total porosity ($n_{T\_\mu CT}$), effective porosity ($n_{eff\_\mu CT}$), isolated porosity ($n_{isol\_\mu CT}$), tortuosity of the pore space (centroid path tortuosity; T), crystallinity, and geometric parameters of vesicles and crystals were quantified using dedicated modules from PerGeos. Objects with less than two pixels in volume or area, which are subject to significant uncertainty (Hughes et al., 2017; Pappalardo et al., 2018), were excluded by a filter analysis. A pore network model (PNM) was also generated for vesicular and fractured prismatic specimens to allow for a visualisation on the internal and connected pore structure. The PNM uses the separated pore space as input and gives a series of pores (spheres with the same volume as the original pore) connected by throats (lines) that form a network. In addition, absolute permeability (k) was calculated for 3D segmented images of prisms and cylinders using the Lattice Boltzmann method and considering a single-phase fluid flow that is simulated by solving the Navier-Stokes equation and applying Darcy's Law (Baker et al., 2012 and references therein). The quantification of porosity and permeability and the creation of PNM are developed using dedicated modules from the PerGeos software.

The label analysis module of PerGeos software calculates numerous parameters (length, width, breadth, thickness, Feret diameter, area, Crofton perimeter, equivalent diameter, Feret shape, shape factor, eccentricity, elongation, anisotropy, roundness, circularity, and sphericity; User's Guide PerGeos Software - PerGeos, 2021 - and Glossary). A principal component analysis (PCA) was conducted on pore space data (2D and 3D) using a varimax rotation with Kaiser normalisation on IBM SPSS statistics 29.0 software to reduce the dataset dimension and obtain the most significant parameters. Representative variables were also considered for the description of phenocrysts. Data analysis and descriptive statistics were conducted in Microsoft Excel®.

3. Results

3.1. Petrographic and geochemical characterisation

IUGS classification (Streckeisen, 1978; Le Maitre et al., 2002) determines that BP and BAf (Sete Cidades volcano) and BF (Fogo volcano) are basalts, and T29 and T31 correspond to trachytes based on the estimated mineral content. Whole-rock chemistry further shows that the samples range from alkali-basalts (BAf and BP; BAf18 is a trachybasalt), basaltic trachyandesite or mugearite (BF3 and BF15), trachyandesite or benmoreite (BF13) to comenditic trachytes (T; Cox et al., 1979; De la Roche et al., 1980; Le Bas et al., 1986). The basalts are ocean island alkaline and derive from intraplate lavas from the Azores. Onwards, mugearites are referred to as basaltic trachyandesites, while benmoreites as trachyandesites. The FMW classification (Ohta and Arai, 2007) indicates that basalts are fresh, while trachytes are slightly altered.

All rocks are holocrystalline with a porphyritic (Fig. 3a) to seriate texture (Fig. 3b), sometimes intergranular (Fig. 3c) and rarely glomeroporphyritic (Fig. 3d), varying from vesicular (BF15, BF13; Fig. 3f) to massive (remaining samples; Fig. 3e). In basalts (*s.l.*), euhedral to anhedral phenocrysts display zoning (Fig. 3g and Fig. 3h), signs of disequilibrium (reaction rim; Fig. 3i), embayments, rare skeletal shape, and a sieve texture of the plagioclase (Fig. 3j), comprising olivine, clinopyroxene, and plagioclase, also present in the fine to medium-grained groundmass together with opaque minerals (titanomagnetite and ilmenite; Fig. 3k). Trachytes also display a trachytic texture (Fig. 3r) with tabular to needle-like alkali-feldspar arranged sub-parallelly. Alkali feldspar (Fig. 3t -; Fig. 3s) exists as phenocrysts or in the groundmass with biotite, opaque minerals, minor amphibole (Fig. 3u), quartz, apatite, and brown clinopyroxene/amphibole (T31; 3w). Basalts are fresh, but it is observed minor oxidation in BAf, and a brown amphibole in the intermediate rocks (BF; Fig. 3l). Trachytes exhibit slight sericitization of feldspar, chloritization of biotite, and the filling of fractures by oxides (Fig. 3x). Massive rocks contain scant microcracks, primarily transgranular to intragranular (Fig. 3e) but fractured varieties (BAf16) show cracks nucleating from intragranular microcracks and vesicles (Fig. 3m). Vesicles in the groundmass are round (Fig. 2n) to coalescent in massive basalts, angular and limited by the feldspar laths in the massive basaltic trachyandesite (BF3; Fig. 3o) and in the trachytes (Fig. 3y). Intracrystalline pores predominate in the sieved plagioclase (Fig. 3p). Vesicular specimens (BF13 and BF15) contain irregular and elongated vesicles, mainly because of coalescence and pore-linking fractures (Fig. 3f).

3.2. Quantification of physical and microstructural features

The analysis strategy involved various multi-scale techniques to examine the full range of vesicles and phenocrysts, yielding complementary but not directly coincident porosity and crystallinity data. 10 samples were analysed under dry conditions (Table 1). Total porosity (n_T) was obtained by point counting (n_{T_PC}) and 2D image analysis for thin sections (n_{T_2D}). Physical properties, namely bulk density and effective porosity were determined for 50 prisms ($\rho_{adp.ISRM}$; $n_{eff\_adp.ISRM}$) and 98 larger irregular lumps (ρ_{ISRM}; n_{eff_ISRM}) based on saturation and buoyancy techniques of ISRM (2007). 3D μCT image analysis yielded $n_{T\_\mu CT}$, absolute permeability (k), and tortuosity (T). Effective porosity obtained by MIP technique (pore radius < 180 μm; n_{eff_Hg}) and μCT ($n_{eff\_\mu CT}$) on the same prisms, complement $n_{eff\_adp.ISRM}$. Phenocrysts content was either quantified in 3D μCT scans of prisms ($Ph_{\mu CT}$) and 2D SEM images of thin sections ($Ph_{2D;\ IA}$), also estimated through point counting in thin sections ($Ph_{2D;\ PC}$).

The buoyancy technique (Table 1) applied on prisms according to ISRM (2007) method, showed that paraffin and the quick water immersion tests are aligned for massive rocks, while paraffin leads to anomalous results on vesicular and fractured samples, where impermeabilisation might be incomplete.

- Alkali basalts (BP and BAf)

BP samples are more porphyritic (16.60 % to 21. 85 % of phenocrysts) than BAf (14.84 % to 16.74 % of phenocrysts), and phenocrysts in thin sections might be less in 1 to 11 % than in 3D digital prisms since dispersed megacrysts might not be captured in thin sections. Local higher porosity zones are displayed, but micropores (radius < 15 μm; Franzson et al., 2010) predominate in these massive samples. The higher resolution used in SEM-BSE scans led to a n_{T_2D} determined through image analysis of BP (5.96 %-8.80 %) and massive BAf (6.38 %-10.70 %) higher than $n_{T\_\mu CT}$.

Irregular lumps and prisms of massive BP basalts show ρ varying from 2.8 to 2.9 g/cm^3, while BAf has ρ from 2.7 to 2.8 g/cm^3. n_{eff} of the basalts goes from 3.5 % to 7 %, showing a good agreement between n_{eff_ISRM} and $n_{eff\_adp.ISRM}$, despite the different specimen size. Rarely (BP38), prisms might not contain connected pore space, which are better represented in the lumps. MIP leads to either lower (BP37), higher (BP38 and BAf14), or similar (BAf18) n_{eff_Hg} than $n_{eff\_adp.ISRM}$, ranging from 2 % to 8 %. BAf16 is distinguished from the remaining basalts given

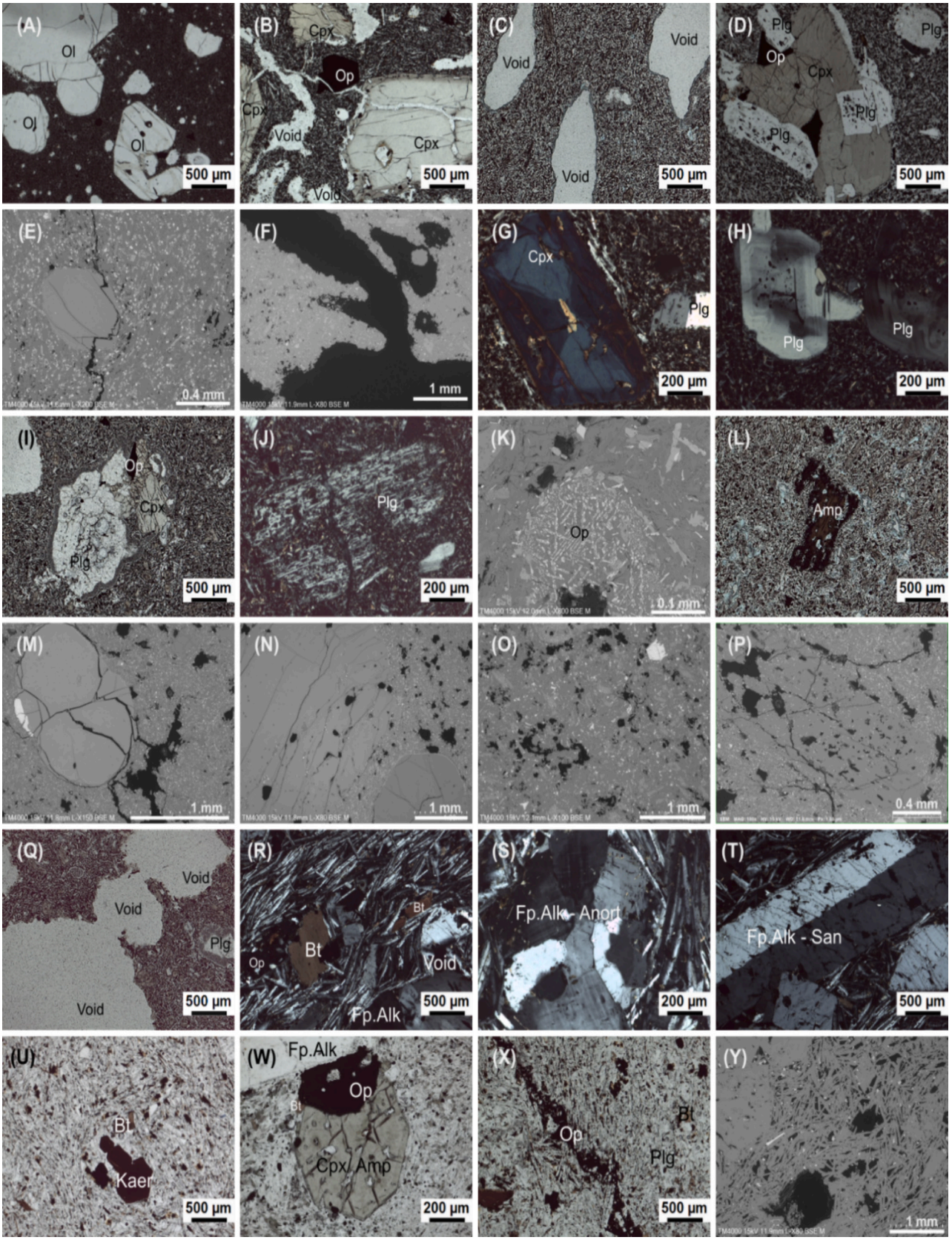

(caption on next page)

Fig. 3. Microphotographs (// - plane-polarised light; X – cross-polarised light) and electron microscope images in backscattered mode (SEM-BSE) of polished thin sections. (A) Porphyritic texture with phenocrysts of olivine and clinopyroxene in a fine-grained groundmass (BP37; //); (B) seriate texture, intergranular with isolated and elongated vesicles (BF13; //); (C) seriate texture, intergranular with isolated and elongated pores (BF13; //); (D) clots of clinopyroxene, plagioclase and opaques – glomeroporpyritic texture (BAf14 //); (E) massive texture with a transgranular fracture with sawed contour (BAf18; SEM-BSE); (F) coalescence of elongated pores (BAf13; BSE); (G) hourglass zoning of clinopyroxene (BAf18; X); (H) zoning of plagioclase (BAf14; X); (I) clot of plagioclase (reaction rim), clinopyroxene and opaque in a vesicular specimen (BAf15; //); (J) disequilibrium of the plagioclase with intense sieve texture (BAf16; //); (K) opaque minerals along the reaction rim of plagioclase (BF3; SEM-BSE); (L) minor brown-amphibole with opaque minerals on its borders (BF3; //); (M) opening of the pre-existing fractures of olivine, connecting to vesicles in the groundmass (BAf16; SEM-BSE); (N) isolated small pores in the groundmass and phenocrysts (BP37; E; SEM-BSE); (O) irregular and angular pores in the groundmass (BF3; SEM-BSE); (P) intracrystalline vesicles connected by transgranular cracks (BAf16; SEM-BSE); (Q) Coalescence of vesicles (BF15; //); (R) trachytic texture and biotite crystal (T29; X); (S) Anorthoclase and (T) Sanidine twinning (T29; X); (U) kaersutite amphibole (T29; //); (W) alteration product with green colour (T31; //); (X) filling of fractures by opaque minerals (T29; //); (Y) pore space limited by the laths of feldspar (T29; SEM-BSE). (For interpretation of the references to colour in this figure legend, the reader is referred to the web version of this article.)

its fractured texture that lowers its ρ (2.4–2.5 g/cm^3) and increases n_{eff_ISRM} and $n_{eff\_adp.ISRM}$ (13.10 %-14.62 %), which show a good agreement despite n_{eff_ISRM} being slightly higher than $n_{eff\_adp.ISRM}$. The BAf16 specimen used for μCT displays a $n_{eff\_\mu CT} = 8.53$ %, $n_{eff\_adp.ISRM} = 13.79$ % and $n_{eff\_Hg} = 17.75$ %, being more permeable (249 mD) than the remaining BAf samples.

- Intermediate lava rocks (BF)

Intermediate lava rocks are less porphyritic than alkali basalts, with 9.36 % to 10.66 % of phenocrysts, with trachyandesite (BF13) having more phenocrysts than the basaltic trachyandesites (BF15 and BF3). Thin sections show more 8 % phenocrysts than the prisms assessed by 3D image analysis. The distinct applied resolution produced a n_{T_2D} higher than the $n_{T\_\mu CT}$ (Table 1); this variation is attenuated for the vesicular specimens, where pores >15 μm become more common.

The massive BF3 has $\rho = 2.6$–2.7 g/cm^3 and $n_{eff\_ISRM} = 7.96$ %, higher than $n_{eff\_adp.ISRM} = 5.90$ % and $n_{eff\_\mu CT} = 6.17$ %. Vesicular varieties (BF15) are less dense (2.2–2.3 g/cm^3), more porous (up to $n_{eff\_ISRM} = 21.85$ %; $n_{eff\_adp.ISRM} = 13.64$ %; $n_{eff\_\mu CT} = 12.64$ %) and more permeable ($k = 13{,}634$ mD) than BF3. BF13 has a density and n_{eff} between BF15 and BF3. $n_{eff\_adp.ISRM}$ is slightly lower than n_{eff_Hg} for the massive BF3, while the opposite occurs for vesicular specimens. $n_{eff\_\mu CT}$ is higher than the remaining methods for vesicular varieties (12.85 %-19.41 %).

- Trachytes (T)

Phenocryst content of trachytes was overestimated by point counting, compared to image analysis of 2D scans and the 3D digital prisms, which feature similar phenocryst content for T29 (~ 19 %) and an 11 % difference for T31 ($Ph_{\mu CT} = 10.23$ %; $Ph_{2D;\ IA} = 21.14$ %). Conversely, n_{T_2D} obtained through point counting and 2D SEM image analysis is similar for both T29 (16.10 %-17 %) and T31 (3.53 % - 3.60 %).

T29 is less dense (2.1–2.2 g/cm^3) and more porous ($n_{eff\_ISRM} = 13.67$ %; $n_{eff\_adp.ISRM} = 8.45$ % for prisms) than T31 (2.5 g/cm^3; $n_{eff\_ISRM} = 4.35$ %; $n_{eff\_adp.ISRM} = 5.09$ %). Trachytic prisms show $n_{eff\_adp.ISRM}$ lower than n_{eff_Hg}, reaching a difference of up to ~8 %. The chosen scale strategy for these microporous samples led to higher $n_{eff\_adp.ISRM}$ and n_{eff_Hg} than $n_{eff\_\mu CT}$.

3.3. Characterisation of the pore space and phenocrysts

3.3.1. Pore size distribution

Mean porous radius, *r*, and pore size distribution (PSD) describe pore structure and are obtained via MIP. Results are depicted in Table 2 and Fig. 4. Independently of the rock nature, texture and structure are the main controllers of *r*. *r* varies from 0.01 to 0.14 μm for massive specimens and reaches a maximum for fractured specimens (BAf16; 0.22 μm), porous trachytes (T29, 0.27 μm), and vesicular specimens (BF15; 0.22 μm). Massive specimens display a prevalence of micropores (pore radius < 15 μm; Franzson et al., 2010) (> 80 %), while the vesicular rocks display more macropores (> 22 %). The vesicular trachyandesite BF13 is an exception as *r* is low compared to the remaining vesicular rocks. Some massive rocks with predominant micropores (e.g., BAf16 and T29) have increased *r* because of existing fractures.

Pore size interval and the cumulative pore volume curves (Fig. 4) reveal that samples BP38 (Fig. 4b) and BAf14 (Fig. 4c) have a single dominant pore family (0.01–0.1 μm) like T29 (0.1–1 μm; Fig. 4i), with the cumulative pore volume curve showing a typical pronounced S-shaped trend. On the other hand, in samples BP37 (Fig. 4a), BAf16 (Fig. 4d), BAf18 (Fig. 4e), BF13 (Fig. 4g) and BF15 (Fig. 4h), the cumulative pore volume curve plotted against pore size exhibits a strong stair-step shape, and in samples BF3 (Fig. 4f) and T31 (Fig. 4j), a smoother stair-step shape, indicating a polymodal pore size distribution and confirming the significant heterogeneity of these rocks.

The pore radius range (0.0015–180 μm) accessible by MIP excludes the complete characterisation of macroporosity associated with vesicles, coalescent vesicles, and fissures. Therefore, for the first time on Azorean rocks, a PNM (Fig. 5) was developed for specimens with connected porosity (Fig. 5a), such as porous (BF13 and BF15) and fractured (BAf16) varieties. BAf16 (Fig. 5b) has a higher number of vesicles (mainly 100 μm equivalent radius) connected by numerous longer throats (length < 100 μm) and a homogenous porosity per slice (Fig. 5a). Conversely, BF13 (Fig. 5c) and BF15 (Fig. 5d) are heterogenous and display porosity peaks coincident with bigger vesicles. These samples contain fewer pores with higher equivalent radii (~ 1000 μm; Fig. SI.2), and volume (> 10^{10} μm^3) that are connected by fewer throats with a channel length distribution more homogenous than BAf16. A maximum channel length in vesicular varieties does not necessarily occur for a higher equivalent radius, contrary to BAf16 (Fig. SI.2). The coordination number of samples (CN – number of nodes connected to each node; Fig. SI.2) shows that most vesicles have one to three openings, with CN > 2 contributing for effective porosity and permeability.

3.3.2. Size and shape of the vesicles and phenocrysts

PCA analysis was conducted on the 2D (thin section; SEM) and 3D (prisms and cylinders; μCT) data, referring to different scales but complementary since variations on the size and shape of these objects throughout rock type follow the same tendency. Three principal components (PC; Fig. SI.3) were considered as they explain 85 % of the variance. PC1 encompasses size metrics in 2D (length, width, Feret diameter, equivalent diameter, area, Crofton perimeter – see the glossary) and 3D (length, width, breadth, thickness, equivalent diameter – see the glossary), together with shape variables (sphericity, shape factor) derived from the volume and surface area. PC2 comprises shape deviation features in 2D (Feret shape, eccentricity, anisotropy, elongation, shape factor or shape_AP) and volume and surface area in 3D. PC3 represents other 2D shape features (circularity and roundness) and shape deviation metrics in 3D (anisotropy, elongation). Length, equivalent diameter, sphericity, and elongation were chosen to characterise pore space and phenocrysts in 3D (Fig. 6a; Fig. 6b) and length, equivalent diameter, elongation, and circularity of pores and phenocrysts in 2D (Fig. 6c; Fig. 6d).

- Alkali basalts (BP and BAf)

Table 1
Average values and number of specimens (N) tested under dry conditions and through distinct methods. *Corresponds to the porosity of the prisms scanned in the μCT. Values for intermediate rocks updated from Pereira et al. (2023a). ρ – dry bulk density; γ- dry unit weight; n_T – total porosity; n_{eff} – effective/ open porosity; n_{isol} – isolated porosity; k –permeability; $\mathcal{T}$ – tortuosity; Ph – phenocrysts; H_2O – quick water immersion technique; Paraff. - paraffin immersion technique; Hg Por. – mercury porosimeter. The areal percentage of crystals and pore space were assessed using point counting and image analysis (PerGeos) of SEM-BSE images. Since two thin sections for each sample of BP and BAf were analysed, quantifications refer to average values. Configurations of prismatic specimens tested in the μCT are in Table SI.1. [a] percentage of vesicles.

Sample	Thin Section				Irregular lumps; ISRM (2007)		Prismatic specimens; ISRM (2007) and electronic densimeter			Prismatic specimen (*); μCT and image analysis						Prismatic specimen (*); Hg Por.
	Point counting (%)		Image analysis (%)		ρ_{ISRM} (kg/m^3)	n_{eff_ISRM} (%)	$\rho_{adp.ISRM}$ (kg/m^3)		$n_{eff\_adp.ISRM}$ (%) ($N = 3$)	$n_{T\_\mu CT}$ (%)	$n_{eff\_\mu CT}$ (%)	$n_{isol\_\mu CT}$ (%)	$\mathcal{T}$	$k_{\_\mu CT}$ (mD)	$Ph_{\mu CT}$ (%)	n_{eff_Hg} (%)
	$Ph_{2D;\ PC}$	$n_{T\_2D;\ PC}$	$Ph_{2D;\ IA}$	$n_{T\_2D;\ IA}$			H_2O ($N = 4$)	Paraff. ($N = 1$)								
Basalt to trachybasalt																
BP37	13.75	4.05	12.96	5.96	2.840 $N = 10$	6.30	2.906	2.859	6.98; 5.37*	2.07	–	–	–	–	16.60	4.08
BP38	9.75	8.80	11.84	8.82	2.840 $N = 11$	5.55	2.808	2.713	2.79; 2.84*	3.92	–	–	–	–	21.85	8.25
BAf14	19.35	5.30	17.79	6.38	2.741 N = 11	3.57	2.796	2.647	3.26; 2.46*	0.97	–	–	–	–	16.74	4.17
BAf16	15.05	12.35	14.14	12.42	2.438 N = 10	13.10	2.479	2.287	14.62; 13.79*	14.33	8.53	5.78	2.92	248.6	14.84	17.75
BAf18	13.40	7.40	13.89	10.70 (4.97[a])	2.723 $N = 7$	5.50	2.808	2.719	6.72; 4.72*	2.20	–	–	–	–	15.43	4.48
Basaltic trachyandesite to trachyandesite																
BF3	23.49	8.27	15.60	8.64	2.596 N = 11	7.96	2.655	2.591	5.90; 4.24*	2.44	–	–	–	–	9.36	6.17
BF13	14.63	24.65	18.03	25.76	2.243 $N = 8$	15.64	2.318	2.155	11.67; 9.66*	19.61	12.85	6.75	2.59	256.2	10.66	8.17
BF15	12.31	29.93	12.70	29.05	2.190 N = 10	21.85	2.196	1.888	13.64*	25.13	19.41	5.71	1.60	13,263.9	5.74	12.64
Trachyte																
T29	27.30	17.00	19.54	16.10	2.145 N = 10	13.97	2.200	2.166	8.45*	3.33	–	–	–	–	19.38	16.06
T31	30.00	3.60	21.14	3.53	2.467 N = 10	4.35	2.463	2.444	5.09; 5.11*	1.29	–	–	–	–	10.23	6.22

Table 2
Mean porous radius, *r*, and pore size interval obtained by mercury intrusion porosimetry (MIP) of lava rocks. 15 μm corresponds to the micropores threshold defined by Franzson et al., 2010.

Sample		r (μm)	Micropores (%) (< 15 μm)	Macropores (%) (≥ 15 μm)	Pore size interval in μm (%)					
					< 0.01	0.01–0.1	0.1–1	1–10	10–100	> 100
Basalt to trachybasalt	BP37	0.14	79.6	19.6	0.0	14.6	12.8	51.2	18.5	2.3
	BP38	0.01	90.9	8.5	5.3	68.0	12.7	4.2	7.3	1.8
	BAf14	0.06	85.6	13.8	0.0	51.8	26.4	6.2	10.8	3.7
	BAf16	0.22	81.6	17.7	0.0	10.9	41.4	26.8	18.2	2.0
	BAF18	0.06	87.6	11.3	0.0	41.8	24.8	19.3	10.3	2.7
Basaltic trachyandesite to trachyandesite	BF3	0.10	94.5	5.0	0.0	21.4	61.7	9.3	6.3	0.9
	BF13	0.03	67.1	30.9	7.6	13.5	12.8	24.6	35.8	3.7
	BF15	0.22	77.8	22.2	0.0	16.7	10.1	40.9	31.0	0.9
Trachyte	T29	0.27	93.9	5.4	0.0	5.8	78.8	8.5	5.0	1.2
	T31	0.04	93.7	6.0	0.0	45.1	30.4	16.4	6.3	0.8

Basalts have 3D vesicles with an average length of <212 μm and equivalent diameter of <56 μm, with elongation and sphericity of 0.42 and 0.84, respectively. BAf16 displays greater length (844 μm) and equivalent radius (155 μm) for connected vesicles and lower sphericity (0.48), indicating fracture-induced pore linking, while elongation remains similar to other alkali basalts. 3D ferromagnesian minerals range from 188 to 351 μm in equivalent radius, with an average elongation of 0.38 and sphericity of 0.58 for basalts. Occasional sphericity reductions are attributed to prevalence of prismatic clinopyroxene (see section 3.1). Plagioclase, only found in BAf basalts, reaches up to 268 μm equivalent radius, with an average sphericity of 0.47 and an average elongation of 0.39.

In 2D, basalts contain vesicles with an average length of 18–25 μm and an average equivalent radius of <8 μm, while their shape has an average circularity of >0.81 and low elongations <0.28. Higher elongation is attained for BAf16, while average circularity remains similar to other basalts. Phenocrysts up to an average length and equivalent radius of 1205 μm and 422 μm, respectively, have 0.28–0.41 of average elongation and 0.25–0.41 of average circularity (Fig. 6d).

- Intermediate lava rocks (BF)

Vesicular samples (BF15 and BF13) have increased average 3D length (1106–1620 μm) and 3D equivalent radius (309–396 μm) than basalts due to connected and coalescent vesicles. They have higher elongation (0.45 to 0.52) and decreased average sphericity (0.59–0.65). Massive basaltic trachyandesite (BF3) and isolated vesicles of BF15 and BF13 reveal average 3D length ~ 150 μm, 3D equivalent radius ~ 32 μm, average 3D elongation of 0.34 and average sphericity of 0.81, akin to massive basalts. Average 3D elongation of ferromagnesian minerals and plagioclase is reduced from basalts to intermediate lavas, contrarily to plagioclase size, reaching an average length of 994 μm. The elongation of this mineral is constant for the intermediate rocks, while the average plagioclase sphericity decreases to 0.39 for the trachyandesite (BF13).

Vesicular rocks (BF15 and BF13) in 2D reinforces the increased average length (30–77 μm) and equivalent radius (9–21 μm) and lower average circularity (0.63) than alkali basalts, contrarily to the massive variety (BF3) that remains similar to the latter (~ 25 μm length, ~ 7 μm equivalent radius, ~ 0.72 circularity). Euhedral plagioclase (section 3.1) leads to a circularity drop, while 2D elongation decreases at a lower extent (0.20–0.25). The trachyandesite (BF13) exhibits the larger phenocrysts (1424 μm in length and 403 μm in equivalent radius).

- Trachytes (T)

Trachytes display average 3D pore lengths (125–144 μm), equivalent radii (28–32 μm), elongation (0.34) and sphericity (0.82), and corresponding 2D features (average 2D length of 21–33 μm, equivalent radii of 6–8 μm, 2D elongation of 0.23, and circularity of 0.65), in agreement with other massive samples. In 2D, the sub-parallel arrangement of feldspar laths limiting vesicles in T29 is responsible for the slight decrease in the circularity of the vesicles.

The phenocrysts show a higher average 3D equivalent radius of alkali-feldspars (169–242 μm) than biotite/amphibole (137–143 μm). Alkali feldspar becomes more elongated (0.31 to 0.39) as sphericity decreases (0.58 to 0.27). The same is not applied to biotite/amphibole. 2D observations confirm an increase in elongated phenocrysts with low circularity compared to other rock types (969–1310 μm in length and 229–375 μm in equivalent radius; 0.03–0.05 in circularity and 0.28–0.32 in elongation).

3.4. Quantification of the mechanical properties and post-deformation physical properties

The UCS samples for X-ray imaging comprise a porphyritic basalt (BAf14), a less porphyritic intermediate lava (BF3), a vesicular intermediate lava (BF13), and a trachyte (T31). Table 3 presents the physical and hydraulic properties of these samples before and after deformation. The coefficient of variation (COV – the ratio between the standard deviation of the grey levels and mean grey level), calculated from μCT greyscale images and referent to the heterogeneity of the samples (Heap et al., 2023), displays similar values amongst rock types. The minimum and maximum COV coincide with the lowest and highest heterogeneity for the basaltic trachyandesite (BF3; COV = 0.049; 1.89 %) and the vesicular trachyandesite (COV = 0.059; n_T = 15.36 %; n_{eff} = 4.10 %; k = 0.5 mD and $\mathcal{T}$ = 1.55), respectively. n_{eff} of massive specimens is influenced by micropores <15 μm, resulting in underestimation and null permeability pre-deformation.

The study reveals that all rocks are brittle, with a steep stress drop after failure (Fig. 7). BAf14 (UCS > 106.24 MPa) did not reach collapse during the UCS test due to the maximum load capacity of the press (5210 N). The massive trachyandesite (BF3; UCS = 80.98 MPa) experienced a strength decrease due to higher plagioclase content than the alkali basalt. Vesicularity led to lower UCS values, with vesicular trachyandesite (BF13; UCS = 21.84 MPa) showing a 3.7-fold strength reduction from BF3. The trachyte (UCS = 77.65 MPa), with alkali-feldspar and amphibole/biotite, was less competent and exhibits greater strain accumulation than the remaining massive samples. BF3 and T31 experienced a stress drop at 40 MPa but showed strength recovery in the elastic regime. Regarding stiffness, independently of the sample, E_{avg} is the highest and E_{tg} the lowest Young's moduli, with E_{sec} averaging between. Stiffness positively relates to UCS, as higher E is found for the more competent basalt, while the vesicular variety exhibits the lower stiffness.

Phenocryst content (Table 3) plays a minor role than the composition of the volcanic rocks on strength. Amongst the massive samples, trachytes exhibit more phenocrysts and lower strength, while BAf14

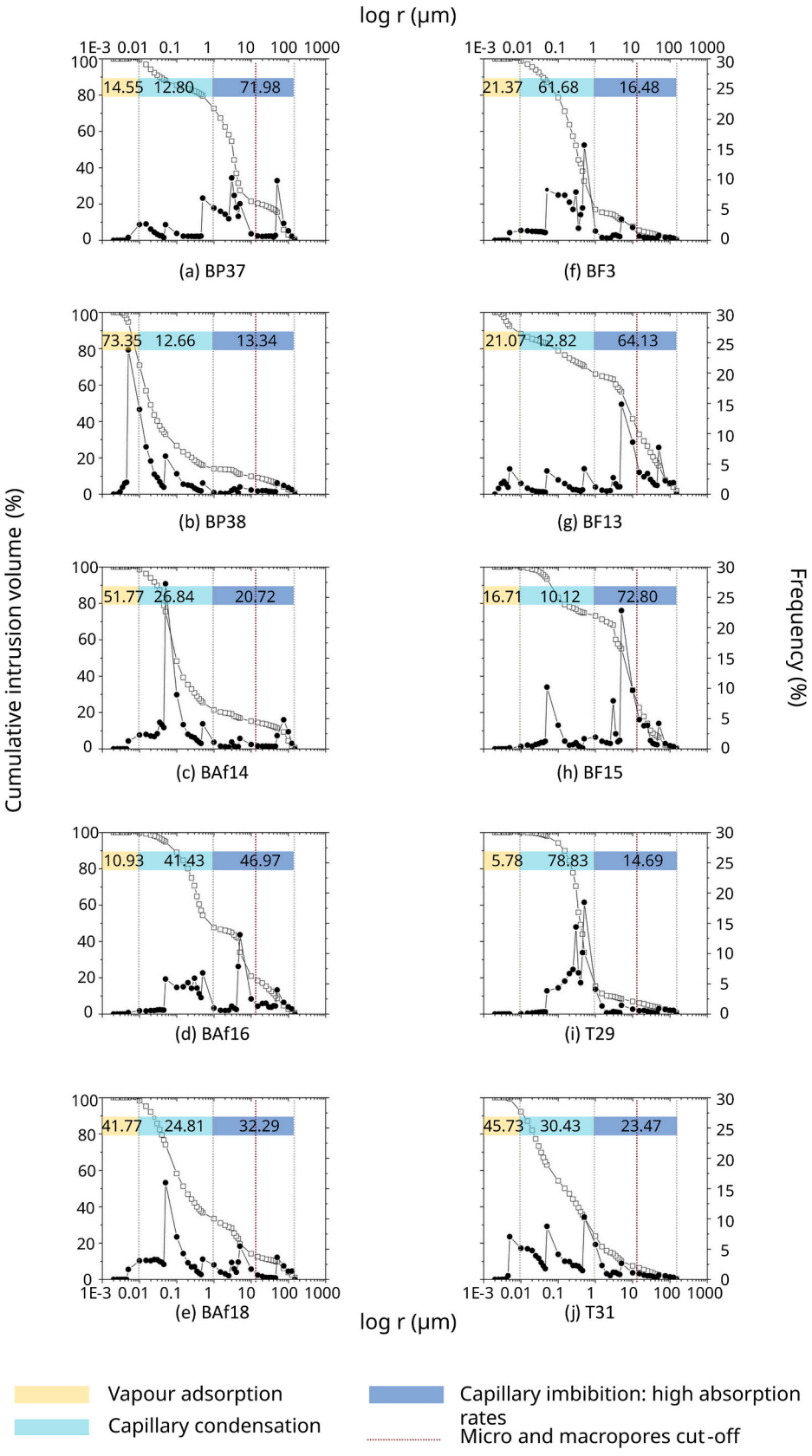

Fig. 4. Cumulative mercury intrusion (empty squares) and pore size distribution (solid circles) curves of the lava rocks. Alkali basalts correspond to (a) BP37, (b) BP38, (c) BAf14, and (d) BAf16. Trachybasalt is (e) BAf18. Intermediate rocks include (f) BF3, (g) BF13, and (h) BF15. Trachytes are (i) T29 and (j) T31. Pore volume curves with a S-shaped trend [(b), (c), (i)] and stair-shaped trend [(a), (d), (e), (f), (g), (h), (j)].

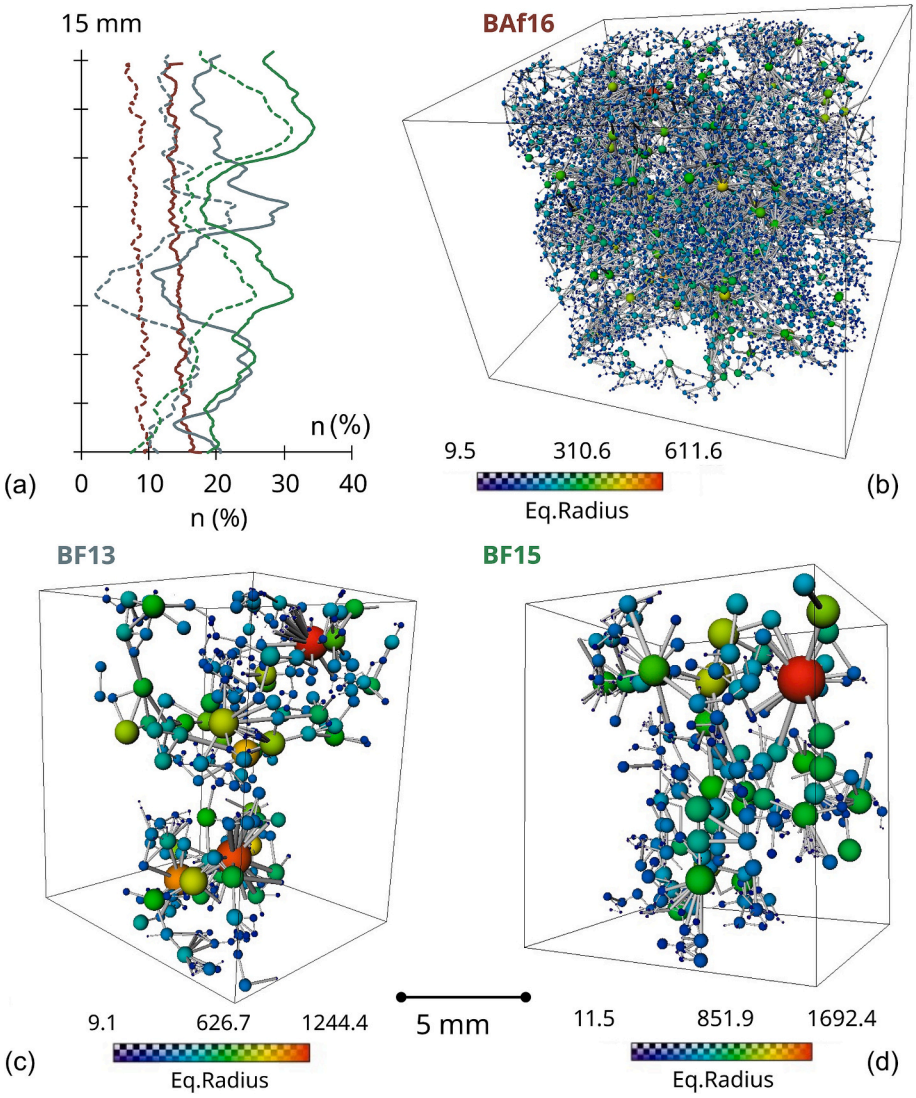

Fig. 5. Pore network models. (a) Porosity variation per slice – connected (dashed line) and total (full line) – and pore network model representations for samples (b) BAf16 – a fractured basalt containing smaller pores connected by a higher number of throats; and (c) BF13 and (d) BF15 that correspond to vesicular specimens with pores of larger size but lower number of throats than BAf16. Pores are represented as a function of their equivalent radius (coloured), and throats are channels, whose width depends on their length (white).

displays high competence despite its porphyritic nature.

Failure modifies the structure, increasing porosity, tortuosity, and permeability (Table 3). Low porosity rocks, like BF3 and T31, can reach $n_T = 12.90$ %, $n_{eff} = 11.56$ %, $k = 43$ mD, $T = 1.50$ and $n_T = 11.34$ %, $n_{eff} = 10.17$ %, $k = 23$ mD, $T = 1.36$, accordingly. Vesicular trachyandesite (BF13) reaches a $n_T = 21.21$ %, $n_{eff} = 9.08$ %, $k = 210$ mD, and $T = 1.35$ after UCS test, which means that effective porosity increases by almost ~5 times, permeability increases by 420 times and the sample becomes less tortuous considering the entire pore space. Higher tortuosity is achieved considering solely the fractures.

Post-deformation imaging (Fig. 7) reveals that under unconfined compression, tensile splitting failure occurs. BF3 shows multiple and extensive cracking, with fracture deviations promoted by pores in the matrix (Fig. 3o) or disequilibrium textures in the feldspar. BF13 crack pattern is conditioned by the elongated macropores connected by cracks that radiate from their edges, showing that elongated macropores facilitate crack nucleation and propagation. In the trachyte, tensile cracks propagate along the boundaries of feldspar phenocrysts parallel to the loading direction. Given the pre-existing intragranular pores and cracks, irregular and dense fracture networks form inside the phenocrysts.

The vertical orientation of pore space and phenocrysts (orientation ϕ) of UCS-tested samples (Fig. SI.4) was analysed in this study. Results show that most vesicles are oblique to perpendicular ($\phi > 40°$) to the axis of the specimen and confirm their sphericity of 0.8–0.9. The inclination of vesicles is independent of their equivalent diameter (and radius) and sphericity and appears to have a minor influence on the strength of the rock. The phenocrysts (Fig. SI.4) in BAf14, BF3 and T31 are mainly oriented perpendicular to the specimens' axis, displaying variable sphericity (all crystals in the trachyte have a low sphericity of ~0.2–0.3) and size regardless of the ϕ. The vesicular intermediate rock (BF13) has homogeneous ϕ for phenocrysts, i.e., large plagioclase minerals are found in various inclinations from the specimen's axis. Thus, contrarily to the vesicularity and mineralogic composition, the orientation of the vesicles and crystals to the axis of the specimen is not correlated with UCS and stiffness of the specimens.

UCS tests were further performed on 45 mm specimens with similar nature, initial open porosity, and dry bulk density (Fig. 8; Table SI.2). Alkali basalts with n_{eff_ISRM} of 4.17 to 4.42 % and a ρ varying from 2.689 to 2.745 g/cm^3 have higher UCS (81.15 to 86.27 MPa) than massive intermediate rocks ($n_{eff\_ISRM} = 9.77$ %; $\rho = 2.500$ g/cm^3; UCS = 77.81 MPa), which, however, display higher stiffness (E = 40–46 GPa) than

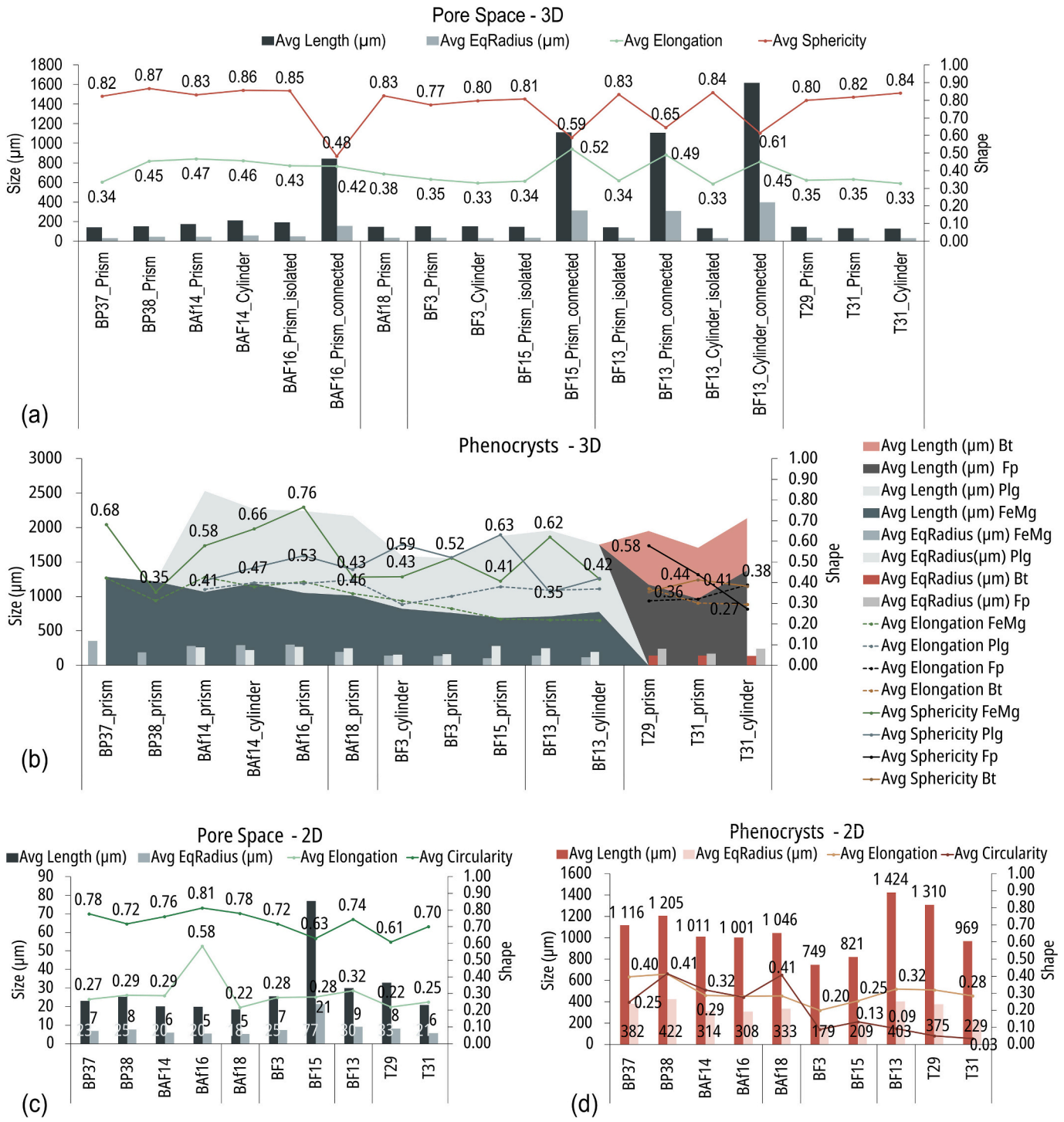

Fig. 6. Characterisation of the microstructure of volcanic rocks from Sete Cidades (BP37; BP38; BAf14; BAf16 – alkali basalt; BAf18 - trachybasalt) and Fogo (BF3; Bf15 – basaltic trachyandesite; BF13 – trachyandesite; T29; T31 - trachyte) volcanoes in three dimensions (a and b) and two dimensions (c and d). (a) average size and shape of vesicles in 3D; (b) average size and shape of phenocrysts in 3D; (c) average size and shape of vesicles in 2D; (d) average size and shape of phenocrysts in 2D. Avg – average; Bt – biotite, FeMg – ferromagnesian minerals; Plg – plagioclase; Fp – Alkali-feldspar.

alkali basalts (E = 36–39 GPa). Contrarily to the 7 mm trachyte, the 45 mm specimens (n_{eff_ISRM} = 2.73–2.89 % and ρ = 2.466–2.567 g/cm^3) are less stiff (E = 27–29 GPa) than the remaining massive samples, while reaching higher values of UCS (87.29 MPa to 153.43 MPa). Thus, increasing feldspar content does not always implicate a strength reduction. The 45 mm vesicular specimen (n_{eff_ISRM} = 15.12 %; ρ = 2.240 g/cm^3) confirms observations for 7 mm scale, i.e., that vesicular texture leads to lower UCS (57.41 MPa) and stiffness (27–28 GPa) than the massive texture. Moreover, the diameter correction to 50 mm (Turk and Dearman, 1986) has produced higher discrepancies in the data amongst the distinct scales, namely by 63 MPa (Fig. 8). Despite similar initial open porosity and density, the mechanical properties vary in different proportions, and no direct comparison can be performed between the two scales.

Table 3
Microstructure (COV – coefficient of variation; Ph – phenocrysts content) and physical properties ($n_{T\_\mu CT}$ - total porosity obtained by the μCT, $n_{eff\_\mu CT}$ – effective porosity obtained by the μCT, k – absolute permeability, and Ƭ – tortuosity) of the cylinders (configuration specifications in Table SI.1.) obtained from representative volcanic rocks from Sete Cidades and Fogo volcanoes amongst the previously studied as prismatic specimens by μCT (Table 1).

	COV	$n_{T\_\mu CT}$ (%)		$n_{eff\_\mu CT}$ (%)		$n_{isol\_\mu CT}$ (%)		Ƭ		k* (mD)		Ph (%)
		Pre	Post	Pre	Post	Pre	Post	Pre	Post	Pre	Post	
BAf14	0.053	2.58	2.58	–	–	2.58	2.58	–	–	–	–	14.97
BF3	0.049	1.89	12.90	–	11.56	1.89	1.29	–	1.50	–	42.6	12.13
BF13	0.059	15.36	21.21[a]	4.10	19.08	11.26	2.13	1.55	1.35[b]	0.5	210.4[c]	6.54
T31	0.050	0.67	11.34	–	10.17	0.67	1.04	–	1.36	–	23.0	20.89

* k was calculated along ZZ axis (height of the specimen).
[a] from 21.21 % of the pore space, 6.24 % are fractures.
[b] the tortuosity considering solely the fractures is increased to 2.16.
[c] fractures contribute with 7.519 mD to the total 210 mD permeability.

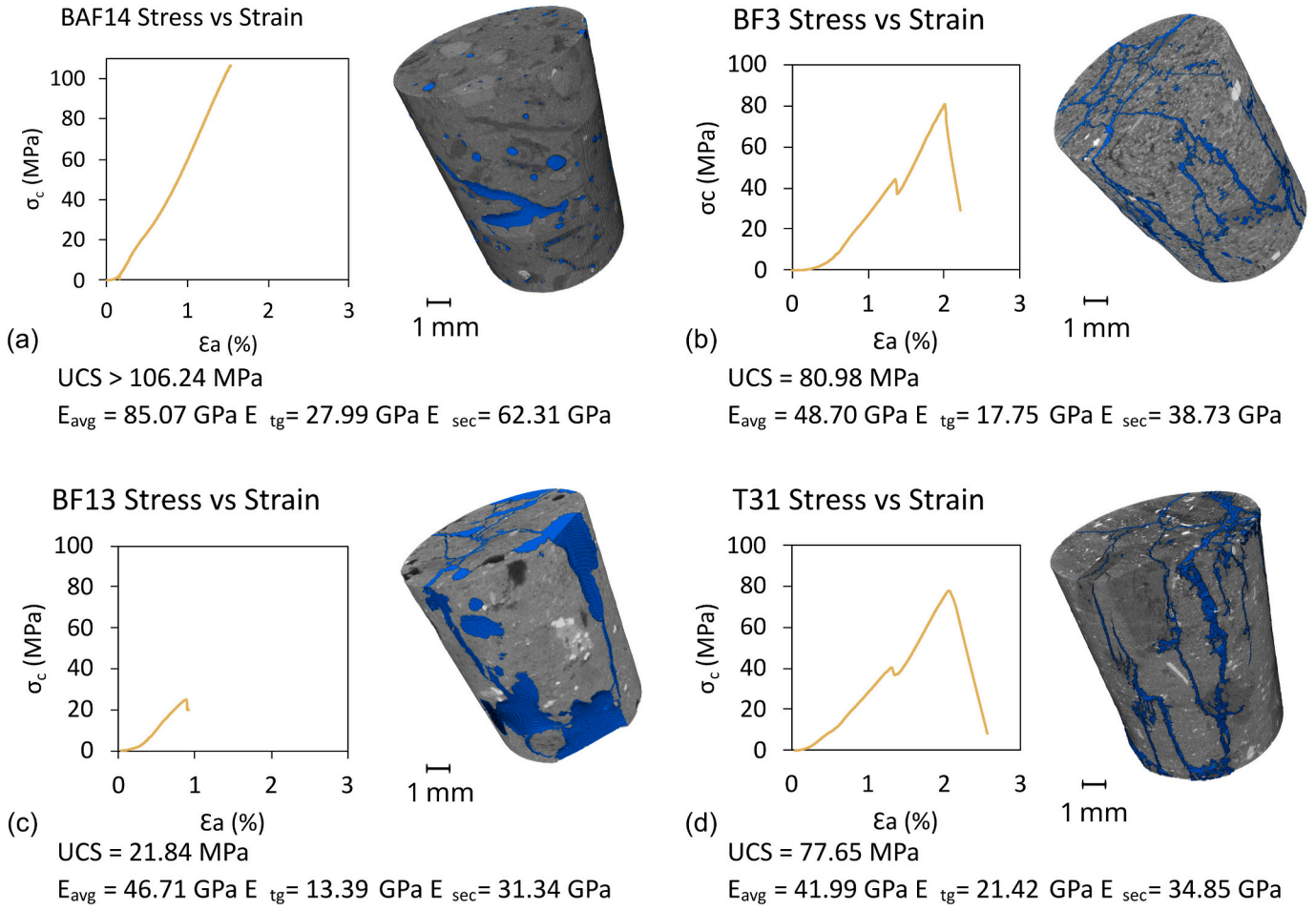

Fig. 7. Stress-strain curves, peak strength, and failure for (a) BAf14: massive basalt specimen with 7.72 mm diameter; (b) BF3: massive basaltic trachyandesite specimen with 7.64 mm diameter; (c) BF13: vesicular trachyandesite specimen with 7.67 mm diameter; and (d) T31: trachyte specimen with 7.69 mm diameter. Connected porosity is represented in blue. (For interpretation of the references to colour in this figure legend, the reader is referred to the web version of this article.)

4. Discussion

4.1. Multi-method and multi-scale approach

The applied methods have been widely used individually in prior studies, but their comprehensive integration remains underexplored, especially in engineering geology contexts. The selected analysis strategy, combining 2D and 3D imaging with laboratory techniques and image analysis, effectively characterises heterogeneous materials like lava rocks. As noted before (Schepp et al., 2020), the resolution plan and varying sample dimensions yield complementary but not coincident results, precluding the estimation of engineering properties through regression analysis in this study. However, the mutual dependence of several index variables is depicted in Fig. SI.5 and Fig. SI.6.

4.1.1. Pore Space and Phenocrysts

μCT allowed to directly visualise and quantify the vesicles and crystals larger than >15 μm, commonly with regular shapes that cannot be accurately defined with conventional 2D techniques. To complement μCT data, smaller vesicles and crystals (< 15 μm), often with a regular

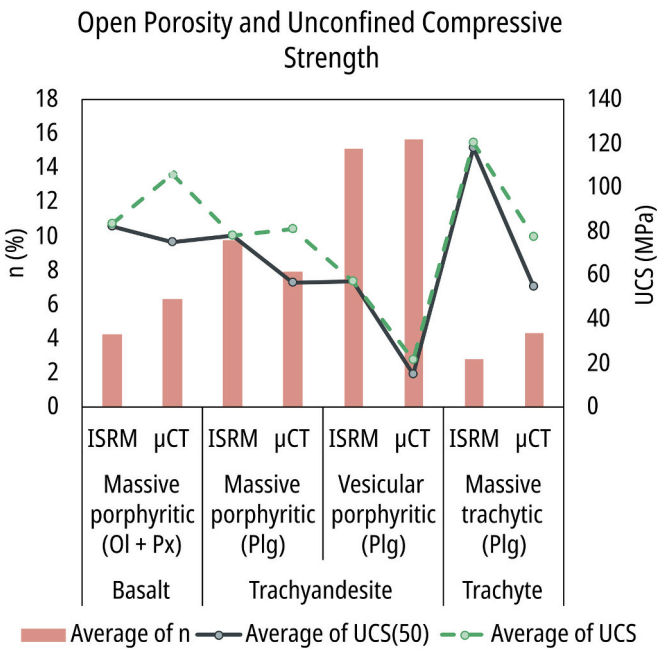

Fig. 8. Multi-scale UCS tests conducted on 45 mm specimens according to ISRM (2007) and on 7 mm specimens scanned with µCT.

spherical shape (e.g., Giachetti et al., 2011; Pappalardo et al., 2018), were assessed by 2D SEM-BSE images that comprise smaller sample portions at higher resolutions. For instance, phenocrysts show size ranges aligned between SEM-BSE and µCT. At the same time, µCT collected an average equivalent radius of ≤396 µm for larger and irregular pores compared to the average size of ≤21 µm for smaller and circular pores in SEM-BSE images. Results reaffirm the variable microstructures of volcanic rocks, comprising microcracks, microporosity, or both (Couves et al., 2016; Griffiths et al., 2017; Cant et al., 2018).

Size and shape of phenocrysts and vesicles inform on processes during the emplacement and cooling of lava rocks, such as overburden and coalescence (e.g., Couves et al., 2016). Indeed, vesicles are relicts of bubbles in magma, which size, shape, and orientation can be changed by several later processes (Shea et al., 2010) that modify their characteristics (Zou, 2013). Their existence in the rock and their size and shape are known to influence deformation, failure, and durability (e.g., Guéguen and Kachanov, 2011), rending volcanic rocks and their rock masses heterogeneous, with implications for the several engineering projects they are concerned.

3D results evidence that vesicles >15 µm of the analysed lava rocks are spheroidal and that their size and shape are independent of the lithology but affected by the texture. Pore coalescence and pore-linking fractures, typical of vesicular lavas, decrease sphericity while elongation increases. Fractures also decrease sphericity, but elongation tends to remain unvaried if the micropores occur in high number and with low elongation (e.g., BAf16). Based on the results, it is suggested that the sphericity of the pore space can be used as a criterion for material selection and considered in future engineering projects since lower rock competence and higher susceptibility to deterioration are expected for rocks with larger and interconnected pores (e.g. Qajar and Arns, 2022; Zhang and Shen, 2023), here characterised by a low average sphericity of the pore space. Elongated pores and interacting voids, such as coalescent vesicles, are inducers of non-uniform stress distribution, favouring stress concentration along their tips and edges (e.g., Jaeger et al., 2009; Davis et al., 2017).

Micropores (< 15 µm) assessed in 2D confirm 3D findings for the pore space, despite the softer variations in the circularity compared to sphericity and more evident reduction of 2D elongation because of fractures than in 3D.

Feldspar laths and prismatic pyroxene in the rock decrease sphericity and circularity of phenocrysts and increase their 2D elongation, while anhedral and rounded olivine increase phenocryst's sphericity.

Point counting might lead to inaccurate values of crystallinity degree for volcanic rocks, given the counting on a distinct scale (groundmass vs. phenocrysts). Image analysis appears as an alternative, but segmenting crystals from the groundmass in volcanic rocks has proved challenging given the similar grey levels (Baker et al., 2012). Texture-supervised classification allowed us to overcome this limitation and quantify phenocrysts, bearing in mind some underestimations by excluding microphenocrysts or overestimations that result from crystal prolongations into the groundmass (BP38).

Total porosity determined by point counting and image analysis (Table 1) on the same thin sections are in agreement (Fig. SI5a), capturing the microvesicles (< 15 µm) that predominate in the massive lavas of S. Miguel Island. Conversely, the fractured basalt (BAf16) is proof that well-distributed fractures are well-predicted in the resolution used in the 3D digital rock, as the $n_{T\_\mu CT}$ is 2.2 % higher than the $n_{T\_2D;\ IA}$ (Fig. SI5b and Fig.SI5c). It is emphasised that µCT combined with image analysis allows the visualisation of internal fractures in rocks not detected by the naked eye, and the definition of the fracture's spatial geometry, not analysable by 2D techniques. Digital rock physics has significance for aggregate and building stone selection as microcracks are regarded as important "defects" within geomaterials (e.g., Pereira et al., 2023b).

Effective porosity is a key parameter in characterising any material used as building stones (e.g., Pappalardo and Mineo, 2017). The wide range of connected porosities in this research (4 % to 22 %; Fig. SI.5) confirms the complex internal pore structure of volcanic rocks, controlled by fractures and coalescence of the vesicles (e.g., Kennedy et al., 2010; Heap et al., 2014a). The connectivity of pores is regarded as a weakening factor of a rock, as confirmed in section 4.1.3., enhancing fluid circulation within the rock (e.g., Bernabé et al., 2010), favouring mixed-mode failure (Heap and Violay, 2021), and making fracture mechanisms more unpredictable. Furthermore, different texture reflects distinct lava flow zones (Couves et al., 2016; Becker et al., 2019), while vesicularity is a function of the magma chemistry, volatile content, and cooling rate (e.g., Walker, 1987). Both texture and number of vesicles influence n_{eff}, while the content of silica and ferromagnesian minerals play a minor role, as previously established (Pereira et al., 2024). Despite the 18 % variance, the obtained results are aligned with those determined for basalts, andesites, and trachytes (Loaiza et al., 2012; Amaral et al., 2018; Malheiro et al., 2018; Pereira et al., 2024 and references therein).

n_{eff} was obtained for the prismatic samples and the irregular lumps. A scale effect affects rocks with n_{eff} > 10 % (BF13, BF15, and T29; Fig. SI5d; Fig. SI5e). The size of prisms might not be enough to retain vesicles and punctual fractures present in the larger irregular lumps, and by omitting rocks with n_{eff} > 10 %, the linear correlation between the different methods would be more effective. Moreover, the number of tested specimens per sample (10 for irregular lumps and three for the prismatic specimens) should be considered as a source of data discrepancy. Vesicular lavas have higher n_{eff_ISRM} and $n_{eff\_adp.ISRM}$ than n_{eff_Hg}, attributed to the combination of the scale effect with the incomplete capture of macropores by the MIP technique. Nevertheless, water intrusion is less efficient for specimens with a single pore family, such as BP38 and T29. Contrarily, the fractured basalt (BAf16) shows higher n_{eff_Hg} than the remaining techniques, evidencing that microcracks are better accessed by mercury than water, probably given the pressure applied in each test.

The MIP technique is crucial for assessing microvesicles, providing a complete PSD under a 180 µm radius. Results show PSD is independent of rock composition, as similar PSD is found for either basalts or trachytes. Vesicular specimens have a strong polymodal PSD, while massive and fractured specimens do not strictly have an unimodal distribution. Furthermore, according to Hölting's classification (Hölting,

1989; Benavente et al., 2015), the throat equivalent radius > 1 mm (Fig. SI.2) found in vesicular specimens suggests an intercrystalline porosity and a permeability controlled by the vesicle size rather than porosity, conversely to the massive, solidified lavas.

Intrinsic and extrinsic factors influence fluid sorption within complex pore systems, with fluids following various kinematic processes due to different mobilising forces (Cueto, 2020). Sorption processes in rocks under subaerial exposure conditions, such as our samples, are described by their respective mechanism (Fort, 1996; Alonso Rodríguez, 2011; Benavente, 2011) and depend on a set of parameters like *r*, PSD, and relative humidity (HR).

For pore radius = 0.0001–0.01 μm and low RH (~ 20 %), a monomolecular layer results from molecules adhesion to the solid surface by electrostatic forces. As RH increases (~ 40 %-60 %), further fluid molecules are adsorbed, creating a multimolecular layer, and fluid movement occurs via surface flow (Rose, 1963), a more efficient transport mechanism than individual molecule diffusion. When RH ~ 75–85 %, pore size ~ 0.1 μm, and the temperature of the porous medium is lower than the dew point of the air, capillary condensation occurs, combining diffusion and capillarity transport mechanisms. Capillary forces bound liquid fluid layers together, which produces a water content that approaches the maximum limits of RH and pore size values (~ 98 % and ~ 1 μm, respectively) for this sorption process. The generation of a continuous liquid phase from any contact with the rock surface is designated by capillary absorption, where fluid is driven by the pressure that results from capillary forces due to the surface tension (Benavente, 2003; Hall and Hoff, 2021). Imbibition kinetics is activated from pore sizes >0.1 μm (Winkler, 1997) but reaches maximum water absorption rates for pores between 1 μm - 1 mm (Benavente et al., 2018). At last, with pore sizes >1 mm, fluid transport becomes governed by hydrodynamic principles, with the gravitational mechanism assuming greater significance (Hall and Hoff, 2021).

In most samples (BP38, BAf14, BAf16, BAf18; BF3; T31), the prevalent pore size ranges between 0.001 and 1 μm (Table 2; Fig. SI.2), which implies that both vapour adsorption and capillary condensation are the governing fluid transport mechanisms. However, condensed fluid can decrease gas diffusion at the surface by obstructing the direct passage of gas (Cueto, 2020). Nonetheless, in a larger volcano-hydrothermal setting scale, the higher temperatures and pressures will favour the gas escape by physical adsorption through the conduit walls (e.g., Jaupart and Allègre, 1991; Heap et al., 2018). Capillary condensation tends to decrease fracture toughness in the rocks (Nara et al., 2012), weakening them and leading possibly to failure, either at a meso- or macroscale. Moreover, such fluid transport can induce rock leaching and secondary mineral precipitation (e.g., Pereira et al., 2024) from the rock mass to the volcano scale, while at the subaerial built environment, massive lava rocks are susceptible to salt crystallisation and prone to deterioration.

Massive basalt samples BP37 and BAf16, and vesicular trachyandesites BF13 and BF15, display pore radii >1 μm (Table 2; Fig. SI.2) and, except for BP37, n_{eff} > 10 %, making them more prone to mechanical failure and fluid circulation within the rock (Benavente et al., 2018). On a volcanic scale, failure renovates permeability with implications for the circulation of hydrothermal and magmatic fluids (e.g., Barreyre et al., 2022), while rapid capillary fluid uptake could also modify soil moisture distribution and influence the flank stability of the volcano (e.g., Baumann et al., 2019). At the surface, the lower mechanical competence and higher susceptibility to deterioration and weathering should be taken into consideration when employing these rocks as building materials and as more sensitive to the typical volcanic and seismic hazards of S. Miguel Island.

4.1.2. Other physical and hydraulic properties

Bulk density negatively correlates with open porosity (Fig. SI.6), as previously established (e.g., Pereira et al., 2022). Notwithstanding, moderate to weak correlations show that density is also a function of the mineralogy, amount of feldspar minerals, and microcracks. For example, basalts BP are denser and equally or more porous than basalts BAf, which contain more plagioclase, confirming that density decreases with increasing feldspar content. Our values are within the range Pereira et al. (2024) established for trachytes and andesites. The structure has a major role, as vesicles promote a density reduction of 0.2 g/cm^3 relative to massive rocks, while fractures can decrease density by almost 0.3 g/cm^3. Bulk density data is retained for specimens with distinct sizes and configurations (Fig. SI.6b), and both water immersion and paraffin immersion methods are relatable (Fig. SI.6c). However, a quick water immersion test is faster and allows for the reuse of the specimens, as paraffin is problematic to remove from the internal structure. Moreover, erroneous values are produced using paraffin for vesicular and fractured rocks.

Permeability is enhanced by vesicular and fractured textures (Fig. SI.2b), with fractures and pore-linking microcracks acting as conduits for fluids. Our findings reaffirm that permeability depends on the type of porosity, as well as its geometry, and tortuosity (Degruyter et al., 2010; Colombier et al., 2017b; Heap et al., 2018; Buono et al., 2020; 2023; Vieira et al., 2021; Liu et al., 2023) but the number of throats contributes more to permeability than the channel length and the size of the vesicles (Fig. 5). Trachyandesites of the Azores (n_{eff} = 18 %; Loaiza et al., 2012) were described as having a mercury porosimeter permeability of 2.736 mD and a mean pore radius of 0.25 μm. The latter is in agreement with the r = 0.22 μm obtained for the tested basaltic trachyandesite (Table 2). However, the computed permeability values largely surpass the permeability established for trachyandesites from the Azores (Loaiza et al., 2012) and fresh andesite lavas (Pereira et al., 2024).

4.1.3. Unconfined compressive strength

Results on the unconfined compressive strength (UCS) demonstrate that all samples are brittle and that texture and structure play a key role. Vesicular texture and higher initial n_{eff} promotes a lower strength. 4D μCT tests show that fracture propagation exploits pre-existing weaknesses, such as vesicles, thin vuggy bands, and intragranular fractures and borders of phenocrysts, as previously established (Tang et al., 2007; Villeneuve et al., 2012; Heap et al., 2014b; Coats et al., 2018; McBeck et al., 2019; Xu et al., 2020; Heap et al., 2023). Our 3D microstructural visualisations show that fractures are mainly pore-emanated in the vesicular trachyandesite and that coalescent pores are preferential features for earlier crack initiation and growth. The low sphericity and the clustering of pores is found to deviate microcracks and possibly can create complex crack patterns under compressive loading, rending intact rock and rock masses failure more unpredictable (e.g., Tang et al., 2000; Reinoso et al., 2019). In massive rocks, nevertheless, fractures propagate mainly through the matrix using pre-existing “defects”, such as phenocryst boundaries and vesicles. For all studied specimens, tensile splitting failure prevails, with fractures propagating according to the wing crack model (e.g., Heap and Wadsworth, 2016).

The presence of feldspar minerals invariably produces low rock density and stiffness, but the effect on strength properties is variable, given the competing role of porosity. For instance, while the weakening effect appears clear for the UCS test performed on a 7 mm cylindric trachyte, the 45 mm specimen showed increased UCS compared to other massive samples.

In this study, most pores are spherical and displayed obliquely to the loading axis (Fig. SI.4.), which does not allow for streamlining clear conclusions about anisotropy. Indeed, in this study, the mineralogy and initial porosity show a major role in the mechanical behaviour compared to the shape and orientation of the vesicles, not sustaining previous studies (Bubeck et al., 2017; Griffiths et al., 2017; Vairé et al., 2024).

The UCS and *E* obtained agree with the values established by Amaral et al. (2018) for vesicular and massive basalts and trachytes. Compared to the data in Pereira et al. (2024), our UCS results align with the UCS of fresh trachytes and are slightly lower than the fresh andesites, while the

static E of these rocks is lower than our Young's moduli. Moreover, the several E produced by the UCS test on 7 mm specimens significantly differ, contrarily to 45 mm specimens. E_{sec} is the most accurate E for the vesicular 7 mm cylinders, and E_{tg} or E_{avg} are more appropriate for massive specimens, being within or closer to the several Young's moduli determined for the 45 mm diameter cylinders. Moreover, strain gauges used in the 45 mm UCS tests are sensitive to rock deformation, contrary to the plate displacement considered for the 7 mm cylinders. Their E should be considered with precaution.

It is expected for the UCS to be more influenced by a size effect than Young's modulus (Hudson and Harrison, 1997). However, the obtained results do not allow for a clear conclusion about a scale effect affecting the strength of specimens with distinct sizes, given the limited number and heterogeneity of the specimens. The size effect is not consensual (e.g., Hoek and Brown, 1980; Hawkins, 1998), but while frequently verified from the rock mass to the intact rock, few studies have focused on this effect from the intact rock to the μCT scale. However, recent research on limestones reveals a good agreement between the UCS for 10 mm and 45–50 mm sized cores (Van Stappen et al., 2019).

4.2. Implications to engineering geology

Basalts, trachyandesites, and trachytes are the composing lava rocks below the volcanoes, volcanic domes, and the Ribeira Grande geothermal field in S. Miguel Island (e.g., Moore, 1991a; Moore, 1991b; Pereira et al., 2022). Consequently, these rocks compose numerous island's slopes and serve as a main georesource for natural stone and aggregate. Understanding their physical and mechanical characterisation has wide-ranging implications for engineering purposes, particularly given their relevance in slope stability, volcanic hazard assessment, and material usage for construction. UCS and E are considered in geomechanical classifications (e.g., Bieniawski, 1989) and used to define the failure criteria for intact rock (e.g., Hoek and Brown, 1980) and estimate in situ stress (e.g., Hudson and Harrison, 1997) and the deformability of fractured rock masses (Hoek and Diederichs, 2006; Yoshinaka et al., 2008). Moreover, physical and mechanical properties are important for building materials and stone conservation (e.g., Benavente et al., 2015; Benavente et al., 2018; Di Benedetto et al., 2015), particularly in seismically and volcanically active environments like S. Miguel.

The adopted analysis strategy, combining conventional and innovative techniques at a micro- to mesoscale, delivers detailed data that supports fundamental studies. For instance, such data can serve as input parameters and improve models predicting failure in heterogenous rock masses (e.g., Reinoso et al., 2019) or destabilization within volcanoes (e.g., Heap et al., 2020b; Heap et al., 2023). Nevertheless, transposing these results to larger-scale volcanoes and geothermal reservoirs remains a nontrivial issue (Heap et al., 2020b; Vairé et al., 2024), given its complexity.

Heterogeneity of the studied volcanic rocks prevails across different scales and is influenced by microcracks, porosity and mineralogy, which directly affect mechanical response. The observed microcracks and fractures represent partially the larger network of discontinuities responsible for the permeability of fractured rock masses or large-scale volcanoes where fractures are ubiquitous (e.g., Heap et al., 2018; Heap et al., 2020b). Notwithstanding, this research clarifies that either intragranular or not, microcracks and vesicles are precursors to the nucleation and propagation of larger discontinuities, favouring strength and stiffness reduction and increasing permeability. Vesicular specimens, whose vesicles are commonly oriented with the flow direction of the lava (Vairé et al., 2024), are here classified as low-strength rocks with an average stiffness (Deere and Miller, 1966) that display connected pore networks characterised by an average low sphericity. This study highlights the importance of n_{eff}, especially when higher than 10 %, and sphericity as critical criteria for preliminary material assessment in engineering applications. The vulnerability of vesicular lava rocks to failure and deterioration by water capillarity and salt crystallisation implies their careful selection for construction purposes and routine inspections to guarantee their performance, especially in seismic regions. At a larger scale, vesicular rocks can lead to slope and volcano flank instability (e.g., Del Potro and Hürlimann, 2008; Ball et al., 2018; Harnett et al., 2018; Acocella, 2021; Heap et al., 2021).

The results also demonstrate that the type of minerals (e.g., ferromagnesian or feldspar minerals) and the rock's texture influence failure mechanisms under unconfined conditions, as previously stated (Fereidooni and Sousa, 2022). Trachytes, although less stiff than basalts, do not consistently have lower UCS due to their initial porosity. Classified as medium- to high-strength rocks (Deere and Miller, 1966), their strength depends on the microstructure, namely the interplay between trachytic texture and microcrack density. In addition, trachytes are more susceptible to weathering given their high alkali-feldspar content, which has implications for their long-term performance and aesthetic as natural stone. This susceptibility also underscores the need to consider hydrothermal alteration in evaluating the stability of trachytic dimes, both locally and globally.

5. Conclusions

This research provides the first comprehensive characterisation of the microstructure of lava rocks from S. Miguel Island and its interaction with key some index properties. The tectonic and volcanic setting of S. Miguel Island pose a significant risk to nearby human settlements, similarly to what is found on other volcanic islands. However, lava rocks constitute important geological-geotechnical units that are extensively exploited. Assessing the engineering properties of volcanic rocks from a micro- to mesoscale is fundamental to fully characterising the complex pore space and understanding the mechanical behaviour based on the microstructure. The following conclusions are drawn:

- Lava flows exhibit diverse compositions and textures. In S. Miguel, dense, low-porosity, and competent porphyritic massive basaltic lavas evolve into intermediate and trachytic lavas with lower strength, density, and higher porosity. Exceptions include vesicular textures or late fracturing, reducing strength and increasing porosity.
- For the first time, the microstructure of Azorean lava rocks has been extensively assessed. The multi-method approach used in this research has proved effective and allowed vast data collection on Azorean lava rocks, characterising both the macro- and microporosity and mechanical properties using laboratorial and digital rock physics techniques.
- Spherical pores are predominant in the volcanic rocks, becoming more angular when constrained by feldspar microlites in the groundmass. Phenocrysts tend to be elongated, and their borders and intracrystalline microcracks and micropores reduce the overall strength of the rock rather than their orientation. No clear conclusion regarding the anisotropic effect of vesicles and phenocrysts can be delineated in this research.
- Sphericity analysis of the pore space in both 2D and 3D effectively documents pore coalescence and the presence of fractures, which contribute to higher rock connectivity, lower competence and durability. Such features are well represented by the used voxel size. It is suggested that together with open porosity and pore size, sphericity of the pore space is used parameter for material characterisation and selection for engineering purposes.
- Thin-section observations are crucial for a preliminary assessment of the mineralogy and texture. Microstructural observations are further enhanced when combined with 3D imaging methods like μCT.
- The use of ISRM (2007) suggested methods is vastly applied to rock mechanics and is much less expensive than the other techniques. It also benefits from a standardised methodology and sample requirement that allow for comparison with values from the literature. ISRM (2007) also delivers information regarding bulk density and can be

adapted to smaller specimens, allowing for a direct comparison to MIP and μCT results. However, some fractures present on irregular lumps might not be collected on the smaller specimens.

- Multi-scale UCS tests can properly and fully describe these rocks, as they are designed for a specific target scale.
- 4D compression tests coupled with μCT are an exciting venue of research in rock mechanics, as they allow to visualise the development of microfractures and their ultimate convergence, resulting in failure. μCT proved to be a versatile and effective technique.
- Digital rock physics enables the determination of key parameters for robust geological and geotechnical studies. The generated pore network models visually represent the internal pore structure, enhancing the understanding of permeability and microstructural data derived from mercury intrusion porosimetry (MIP).
- All tested rocks are brittle and follow a tensile failure under unconfined compression. Deviations in the extensile crack pattern are associated with primary pores, coalescent pores, pore clusters within crystals, pore-linking fractures, intragranular cracks, and phenocryst borders. These act as pre-existing weaknesses exploited by the rock failure, inducing early strength and stiffness loss when predominant.
- Vesicular texture reduces the strength and stiffness of lava rocks and lead to low-strength geotechnical units, with implications for the instability of fractured rock masses and the performance and durability of used natural stones.
- Rocks composing the core of lava flows are massive with a predominance of micropores. Despite being a medium- to high-strength unit, their pore size distribution allows for deterioration over time.
- Vesicle size controls permeability for vesicular lava rocks, with fluid circulation within the intact rock favoured by pore radii >1 mm. Massive lavas with low porosity (n_{eff} < 10 %) tend to have a permeability controlled by their porosity.

Our findings not only benchmark similar lithologies but also provide critical experimental data that can be used in future research. For instance, advanced numerical models, including pores and phenocrysts of different sizes and shapes, could be developed to predict the engineering properties of volcanic materials and better comprehend how the brittle deformation evolves in the rock. Furthermore, the obtained results support and contribute to both practical and theoretical advancements in geotechnical and geological research.

5.1. Glossary

Anisotropy – one minus the ratio of the smallest to the largest eigenvalue of the covariance matrix, measuring the deviation of a region from a sphere.

Area – area of the object or of the object boundary.

Breadth – largest distance, in a plane orthogonal to the maximum Feret diameter, between two parallel lines touching the object but not intersecting it.

Circularity – defines the proximity of the boundary of a particle to a perfect circle (Eq. 1).

$$Circularity = \frac{4\pi Area}{CroftonPerimeter^2} \quad (1)$$

Crofton perimeter – average of four *VarDiameter* measures, which are the product of *intercept(i)* with the distance between interception points. This measure is preferred for measuring object perimeters.

Eccentricity – deviation of a conic section (circle, ellipse, etc.) from a circular shape, reaching the value zero for a true circle.

Elongation – ratio between the largest eigenvalue of the covariance matrix, with elongate objects having values close to zero.

Equivalent diameter – the diameter of the circle of same area (2D; Eq. 2) or of the sphere of same volume (3D; Eq. 3). The equivalent radius is half of the equivalent diameter.

$$EqD = \sqrt{\frac{4\ Area}{\pi}} \quad (2)$$

$$EqD = \sqrt[3]{\frac{6\ Volume}{\pi}} \quad (3)$$

Feret diameter - the length of the Bounding Boxes distributed along the designated directions, describing how “wide” an object is in a given direction.

Feret shape – ratio between b/a, where a is the minimal Feret diameter and b is the Feret diameter closest to the normal of the minimal Feret diameter.

Lava rocks (also solidified lavas) - general term used to refer to a rock that results from the solidification of a lava flow.

Length – maximum of the Feret diameters.

Roundness – defines the deviation of the surface of a particle from a true circle (Eq. 4).

$$Roundness = 4\left(\frac{Area}{\pi Length^2}\right) \quad (4)$$

Shape factor – measure that describes the shape, not being affected by the dimensions of an object and described by Eq. 5 in 2D and Eq.6 in 3D.

$$SF\_2D = \frac{CroftonPerimeter^2}{4\pi Area} \quad (5)$$

$$SF\_3D = \frac{Area^3}{36\pi Volume^2} \quad (6)$$

Sphericity – defines the proximity of a particle to a sphere (Eq. 7).

$$Sphericity = \frac{\pi^{\frac{1}{3}}(6Volume)^{\frac{2}{3}}}{Area} \quad (7)$$

Thickness – largest distance, in a plane orthogonal to the maximum Feret diameter, that touches an object by its end points.

Width – minimum of the Feret diameters.

Funding

The project that gave rise to these results received the support of a fellowship from”la Caixa” Foundation (ID 100010434). The fellowship code is LCF/BQ/DR22/11950029. This project has also received funding from the European Union’s Horizon 2020 research and innovation programme under grant agreement No 101005611 for Transnational Access conducted at Istituto Nazionale di Geofisica e Vulcanologia – Osservatorio Vesuviano (INGV-OV) within the EXCITE project and by the Portuguese Fundação para a Ciência e a Tecnologia (FCT) I.P./ MCTES through national funds (PIDDAC) – UIDB/50019/2020 (https://doi.org/10.54499/UIDB/50019/2020), UIDP/50019/2020 (https://doi.org/10.54499/UIDP/50019/2020) and LA/P/0068/2020 (https://doi.org/10.54499/LA/P/0068/2020). The authors are also grateful for the financial support provided by the European Union - Next Generation EU, by the Spanish Ministry of Universities and the University of Alicante (project reference: MARSALAS22–09), and by the Autonomous Region of Madrid’s Top Heritage Programme (S2018/ NMT-4372).

Declaration of generative AI in scientific writing

During the preparation of this work, the authors used ChatGPT 3.5 for the management of references and Grammarly (Premium) to improve the readability and language of the text. After using these tools, the authors reviewed and edited the content as needed and assumed full responsibility for the content of the publication. To ensure the text’s originality, several sections were put through the AI detector Scribbr,

and the entire document was reviewed by the plagiarism software Ouriginal (Urkund). The manuscript has 18 % similarity, according to Ouriginal, which matches to references and citations in the text.

CRediT authorship contribution statement

Maria Luísa Pereira: Writing – original draft, Visualization, Investigation, Formal analysis, Data curation, Conceptualization. **Lucia Pappalardo:** Writing – review & editing, Supervision, Methodology, Investigation. **Gianmarco Buono:** Writing – review & editing, Methodology, Investigation. **Nora Cueto:** Writing – review & editing, Visualization, Methodology, Investigation, Data curation. **Carmen Vázquez-Calvo:** Writing – review & editing, Methodology, Investigation, Data curation. **Rafael Fort:** Writing – review & editing, Methodology, Investigation, Data curation. **Matilde Costa e Silva:** Writing – review & editing. **Isabel Fernandes:** Writing – review & editing, Supervision. **Vittorio Zanon:** Writing – review & editing, Supervision. **Paulo Amaral:** Writing – review & editing.

Declaration of competing interest

The authors declare that they have no known competing financial interests or personal relationships that could have appeared to influence the work reported in this paper.

The authors have no competing interests to declare relevant to this article's content. The work hereby presented has not been published previously, is not under consideration for publication elsewhere, and all authors approve its publication. If accepted, it will not be published elsewhere in the same form, in English or any other language, including electronically without the written consent of the copyright-holder.

Appendix A. Supplementary data

Supplementary data to this article can be found online at https://doi.org/10.1016/j.enggeo.2025.107907.

Data availability

Data will be made available on request.

References

Acocella, V., 2021. Volcano flank instability and collapse. In: Volcano-Tectonic Processes. Advances in Volcanology. Springer, Cham. https://doi.org/10.1007/978-3-030-65968-4_6.

Alonso Rodríguez, J., 2011. El agua en los materiales rocosos. Open Course Ware Univ Oviedo, p. 12 (in Spanish).

Amaral, P., Malheiro, A., Teixeira, L., Vieira de Sousa, J., Jubera, J., Hernández, L., González de Vallejo, L., Leyva, S., Miranda, A., Victória, S., Delgado, A., 2018. Geomechanical Characterization of Volcanic Materials of Azores and Madeira Archipelago. In: EGU General Assembly Conference Abstracts, p. 15997.

ASTM D7012–23, 2023. Standard Test Methods for Compressive Strength and Elastic Moduli of Intact Rock Core Specimens under Varying States of Stress and Temperatures. ASTM International.

Baker, D.R., Mancini, L., Polacci, M., Higgins, M.D., Gualda, G.A.R., Hill, R.J., Rivers, M. L., 2012. An introduction to the application of X-ray microtomography to the three-dimensional study of igneous rocks. Lithos 148, 262–276.

Ball, J.L., Taron, J., Reid, M.E., Hurwitz, S., Finn, C., Bedrosian, P., 2018. Combining multiphase groundwater flow and slope stability models to assess stratovolcano flank collapse in the Cascade Range. J. Geophys. Res. Solid Earth 123 (4), 2787–2805.

Barone, G., Mazzoleni, P., Pappalardo, G., Raneri, S., 2015. Microtextural and microstructural influence on the changes of physical and mechanical proprieties related to salts crystallization weathering in natural building stones. The example of Sabucina stone (Sicily). Constr. Build. Mater. 95, 355–365doi. https://doi.org/10.1016/j.conbuildmat.2015.07.131.

Barreyre, T., Parnell-Turner, R., Wu, J.N., Fornari, D.J., 2022. Tracking crustal permeability and hydrothermal response during seafloor eruptions at the East Pacific rise, 9°50'N. Geophys. Res. Lett. 49 (3).

Baumann, V., Bonadonna, C., Cuomo, S., Moscariello, M., Biass, S., Pistolesi, M., Gattuso, A., 2019. Mapping the susceptibility of rain-triggered lahars at Vulcano island (Italy) combining field characterization, geotechnical analysis, and numerical modelling. Nat. Hazards Earth Syst. Sci. 19 (11), 2421–2449.

Becker, M., Lima, E.F., Waichel, B.L., Mantovani, I., 2019. Pore system quantification and characterization in volcanic rocks: a case study from the lower cretaceous Serra Geral Group, Parana Basin, southern Brazil. J. Pet. Geol. 42 (3), 301–317. https://doi.org/10.1111/jpg.12735.

Benavente, D., 2003. Modelización y estimación de la durabilidad de materiales pétreos porosos frente a la cristalización de sales. Universidad de Alicante (in Spanish).

Benavente, D., Pla, C., Cueto, N., Galvañ, S., Martínez-Martínez, J., García-del-Cura, M. A., Ordóñez, S., 2015. Predicting water permeability in sedimentary rocks from capillary imbibition and pore structure. Eng. Geol. 195, 301–311. https://doi.org/10.1016/j.enggeo.2015.06.003.

Benavente, D., 2011. Why pore size is important in the deterioration of porous stones used in the built heritage. Macla 15, 41–42.

Benavente, D., Martinez-Martinez, J., Cueto, N., Ordóñez, S., Garcia-del-Cura, M.A., 2018. Impact of salt and frost weathering on the physical and durability properties of travertines and carbonate tufas used as building material. Environ. Earth Sci. 77 (4), 147. https://doi.org/10.1007/s12665-018-7339-0.

Bernabé, Y., Li, M., Maineult, A., 2010. Permeability and pore connectivity: a new model based on network simulations. J. Geophys. Res. Solid Earth 115 (B10). https://doi.org/10.1029/2010JB007444.

Bieniawski, Z.T., 1989. Engineering Rock Mass Classifications: A Complete Manual for Engineers and Geologists in Mining, Civil, and Petroleum Engineering. John Wiley & Sons.

Bubeck, A., Walker, R.J., Healy, D., Dobbs, M., Holwell, D.A., 2017. Pore geometry as a control on rock strength. Earth Planet. Sci. Lett. 457, 38–48. https://doi.org/10.1016/j.epsl.2016.09.050.

Buono, G., Fanara, S., Macedonio, G., Palladino, D.M., Petrosino, P., Sottili, G., Pappalardo, L., 2020. Dynamics of degassing in evolved alkaline magmas: Petrological, experimental and theoretical insights. Earth Sci. Rev. 211, 103402. https://doi.org/10.1016/j.earscirev.2020.103402.

Buono, G., Caliro, S., Macedonio, G., Allocca, V., Gamba, F., Pappalardo, L., 2023. Exploring microstructure and petrophysical properties of microporous volcanic rocks through 3D multiscale and super-resolution imaging. Sci. Rep. 13 (1), 6651.

Cant, J.L., Siratovich, P.A., Cole, J.W., Villeneuve, M.C., Kennedy, B.M., 2018. Matrix permeability of reservoir rocks, Ngatamariki geothermal field, Taupo Volcanic Zone, New Zealand. Geotherm. Energy 6, 1–28.

Cnudde, V., Boone, M., 2013. High-resolution X-Ray computed tomography in geosciences: a review of the current technology and applications. Earth Sci. Rev. 123, 1–17.

Coats, R., Kendrick, J.E., Wallace, P.A., Miwa, T., Hornby, A.J., Ashworth, J.D., Matsushima, T., Lavallée, Y., 2018. Failure criteria for porous dome rocks and lavas: a study of Mt. Unzen, Japan. Solid Earth 9 (6), 1299–1328. https://doi.org/10.5194/se-9-1299-2018.

Colombier, M., Wadsworth, F.B., Gurioli, L., Scheu, B., Kueppers, U., Di Muro, A., Dingwell, D.B., 2017a. The evolution of pore connectivity in volcanic rocks. Earth Planet. Sci. Lett. 462, 99–109. https://doi.org/10.1016/j.epsl.2017.01.01.

Colombier, M., Gurioli, L., Druitt, T.H., et al., 2017b. Textural evolution of magma during the 9.4-ka trachytic explosive eruption at Kilian Volcano, Chaîne des Puys, France. Bull. Volcanol. 79, 17. https://doi.org/10.1007/s00445-017-1099-7.

Couves, C., Roberts, S., Racey, A., Troth, I., Best, A., 2016. Use of X-ray computed tomography to quantify the petrophysical properties of volcanic rocks: a case study from Tenerife. Canary Islands. J Pet Geol 39 (1), 79–94.

Cox, K.G., Bell, J.D., Pankhurst, R.J., Pankhurst, 1979. The Interpretation of Igneous Rocks. Allen and Unwin, London, p. 450. https://doi.org/10.1007/978-94-017-3373-1.

Crawford, K.M., 2013. Determination of Bulk Density of Rock Core Using Standard Industry Methods (Master's Report). Michigan Technological University.

Cueto, N., 2020. Major Controlling Factors on Fluid Transport Properties in Complex Marine and Freshwater Carbonate Rocks: An Integrated Experimental and Theoretical Study on the Relation between Permeability and Capillarity. Ph.D. Thesis,. University of Alicante, Alicante, Spain, p. 406. http://hdl.handle.net/10045/114153.

D'Araújo, J., Sigmundsson, F., Ferreira, T., Okada, J., Lorenzo, M., Silva, R., 2022a. Plate boundary deformation and volcano unrest at the Azores triple junction determined from continuous GPS measurements, 2002–2017. J. Geophys. Res. Solid Earth 127 (1). https://doi.org/10.1029/2021JB023007.

D'Araújo, J., Sigmundsson, F., Ferreira, T., Okada, J., Lorenzo, M., Silva, R., Larrea, R., Gaspar, J.L., 2022b. Multiple inflation and deflation events from 2004 to 2016 at Fogo (Água de Pau) volcano, São Miguel, Azores. J. Volcanol. Geotherm. Res. 432, 107694. https://doi.org/10.1016/j.jvolgeores.2022.107694.

Davis, T., Healy, D., Bubeck, A., Walker, R., 2017. Stress concentrations around voids in three dimensions: the roots of failure. J. Struct. Geol. 102, 193–207. https://doi.org/10.1016/j.jsg.2017.07.013.

Deere, D.U., Miller, R.P., 1966. Engineering classifcation and index properties for intact rock. Air Force Weapons Laboratory Technical, Report AFWL-TR-65-116.

De la Roche, H., Leterrier, J., Grandclaude, P., Marchal, M., 1980. A Classification of Volcanic and Plutonic Rocks Using R1-R2 Diagrams and Major Element Analyses - Its Relationships with Current Nomenclature. Chem. Geol. 29, 183–210.http. https://doi.org/10.1016/0009-2541(80)90020-0.

Degruyter, W., Burgisser, A., Bachmann, O., Malaspinas, O., 2010. Synchrotron X-ray microtomography and lattice Boltzmann simulations of gas flow through volcanic pumices. Geosphere 6 (5), 470–481. https://doi.org/10.1130/GES00555.1.

Del Potro, R., Hürlimann, M., 2008. Geotechnical classification and characterisation of materials for stability analyses of large volcanic slopes. Eng. Geol. 98 (1–2), 1–17.

Di Benedetto, C., Cappelletti, P., Favaro, M., Graziano, S.F., Langella, A., Calcaterra, D., Colella, A., 2015. Porosity as key factor in the durability of two historical building

stones: Neapolitan Yellow Tuff and Vicenza Stone. Eng. Geol. 193, 310–319. https://doi.org/10.1016/j.enggeo.2015.05.006.
Dvorkin, J., Derzhi, N., Diaz, E., Fang, Q., 2011. Relevance of computational rock physics. Geophys 76 (5), E141–E153. https://doi.org/10.1190/geo2010-0352.1.
Fan, L.F., Gao, J.W., Wu, Z.J., Yang, S.Q., Ma, G.W., 2018. An investigation of thermal effects on micro-properties of granite by X-ray CT technique. Appl. Therm. Eng. 140, 505–519.
Fereidooni, D., Sousa, L., 2022. Predicting the engineering properties of rocks from textural characteristics using some soft computing approaches. Materials 15 (22), 7922.
Fort, R., 1996. El agua en los materiales pétreos: comportamiento hídrico. In: Mingarro Martín, F. (Ed.), Degrad. y Conserv. del Patrim. Arquit. cursos verano El Escorial la Univ. Complut. Madrid, 1994, Editorial Complutense, Madrid, pp. 237–248.
Franzson, H., Gudfinnsson, G.H., Helgadottir, H.M., Frolova, J., 2010. Porosity, density and chemical composition relationships in altered Icelandic hyaloclastites. Water-Rock Interaction - Birkle & Torres-Alvarado (eds) 2010 Taylor & Francis Group, London, pp. 199–202. ISBN 978-0-415-60426-0.
Gaspar, J.L., Queiroz, G., Ferreira, T., Medeiros, A.R., Goulart, C., Medeiros, J., 2015. Earthquakes and volcanic eruptions in the Azores region: Geodynamic implications from major historical events and instrumental seismicity. In: Gaspar, J.L., Guest, J.E., Duncan, A.M., FJAS, Barriga, Chester, D.K. (Eds.), Volcanic geology of São Miguel Island (Azores Archipelago), 44. Geol. Soc. Lond. Mem, pp. 33–49. https://doi.org/10.1144/M44.4.
GeothermEx, 2008. Update of the conceptual and numerical model of the Ribeira Grande geothermal reservoir, São Miguel, Azores. In: GeothermEx Inc., report for Sociedade Geotérmica dos Açores, S.A. (SOGEO), p. 190.
Giachetti, T., Burgisser, A., Arbaret, L., Druitt, T.H., Kelfoun, K., 2011. Quantitative textural analysis of Vulcanian pyroclasts (Montserrat) using multi-scale X-ray computed microtomography: comparison with results from 2D image analysis. Bull. Volcanol. 73, 1295–1309. https://doi.org/10.1016/j.jvolgeores.2010.04.001.
González de Vallejo, L., Ferrer, M., 2011. Geological Engineering. CRC Press, Balkema, Leiden, p. 698.
Griffiths, L., Heap, M.J., Xu, T., Chen, C.F., Baud, P., 2017. The influence of pore geometry and orientation on the strength and stiffness of porous rock. J. Struct. Geol. 96, 149–160. https://doi.org/10.1016/j.jsg.2017.02.006.
Guéguen, Y., Kachanov, M., 2011. Effective elastic properties of cracked rocks—an overview. Mechan. Crustal Rocks 73–125.
Hall, C., Hoff, W., 2021. Water Transport in Brick, Stone and Concrete. Spon Press, London.
Hamdi, E., Lafhaj, Z., 2013. Microcracking based rock classification using ultrasonic and porosity parameters and multivariate analysis methods. Eng. Geol. 167, 27–36.
Harnett, C.E., Benson, P.M., Rowley, P., Fazio, M., 2018. Fracture and damage localization in volcanic edifice rocks from El Hierro, Stromboli and Tenerife. Sci. Rep. 8 (1), 1942. https://doi.org/10.1038/s41598-018-20442-w.
Hawkins, A.B., 1998. Aspects of rock strength. Bull Eng Geol Environ 57:17–30 Heap, M. J., and Kennedy, B. M. (2016). Exploring the scale-dependent permeability of fractured andesite. Earth Planet. Sci. Lett. 447, 139–150.
Heap, M.J., Violay, M.E., 2021. The mechanical behaviour and failure modes of volcanic rocks: a review. Bull. Volcanol. 83 (5), 1–47.
Heap, M.J., Wadsworth, F.B., 2016. Closing an open system: Pore pressure changes in permeable edifice rock at high strain rates. J. Volcanol. Geotherm. Res. 315, 40–50.
Heap, M.J., Xu, T., Chen, C.F., 2014a. The influence of porosity and vesicle size on the brittle strength of volcanic rocks and magma. Bull. Volcanol. 76, 1–15.
Heap, M.J., Lavallée, Y., Petrakova, L., Baud, P., Reuschlé, T., Varley, N.R., Dingwell, D. B., 2014b. Microstructural controls on the physical and mechanical properties of edifice-forming andesites at Volcán de Colima, Mexico. J. Geophys. Res. Solid Earth 119, 2925–2963. https://doi.org/10.1002/2013JB010521.
Heap, M.J., Reuschlé, T., Farquharson, J.I., Baud, P., 2018. Permeability of volcanic rocks to gas and water. J. Volcanol. Geotherm. Res. 354, 29–38.
Heap, M.J., Baud, P., McBeck, J.A., Renard, F., Carbillet, L., Hall, S.A., 2020a. Imaging strain localisation in porous andesite using digital volume correlation. J. Volcanol. Geotherm. Res. 404, 107038.
Heap, M.J., Villeneuve, M., Albino, F., Farquharson, J.I., Brothelande, E., Amelung, F., Got, J.L., Baud, P., 2020b. Towards more realistic values of elastic moduli for volcano modelling. J. Volcanol. Geotherm. Res. 390, 106684. https://doi.org/10.1016/j.jvolgeores.2019.106684.
Heap, M.J., Baumann, T., Gilg, H.A., Kolzenburg, S., Ryan, A.G., Villeneuve, M.C., et al., 2021. Hydrothermal alteration can result in pore pressurization and volcano instability. Geology 49, 1348–1352. https://doi.org/10.1130/G49063.1.
Heap, M.J., Meyer, G.G., Noël, C., Wadsworth, F.B., Baud, P., Violay, M.E., 2022. The permeability of porous volcanic rock through the brittle-ductile transition. J. Geophys. Res. Solid Earth 127 (6).
Heap, M.J., Harnett, C.E., Nazarbayov, T., Heng, Z., Baud, P., Xu, T., Rosas-Carbajal, M., Komorowski, J.C., 2023. The influence of heterogeneity on the strength of volcanic rocks and the stability of lava domes. Bull. Volcanol. 85 (9), 49.
Higgins, M.D., 2000. Measurement of crystal size distributions. Am. Mineral. 85, 1105–1116.
Higgins, M.D., 2006. Quantitative Textural Measurements in Igneous and Metamorphic Petrology. Cambridge University Press, Cambridge, UK.
Hoek, E., Brown, E.T., 1980. Underground Excavations in Rock. CRC Press.
Hoek, E., Diederichs, M.S., 2006. Empirical estimation of rock mass modulus. Int. J. Rock Mech. Min. Sci. 43 (2), 203–215.
Hölting, B., 1989. Hydrogeology. An Introduction to General and Applied Hydrogeology. F. Enke Publ, Stuttgart.
Hudson, J.A., Harrison, J.P., 1997. Engineering Rock Mechanics: An Introduction to the Principles. Elsevier Science.
Hughes, E.C., Neave, D.A., Dobson, K.J., Withers, P.J., Edmonds, M., 2017. How to fragment peralkaline rhyolites: observations on pumice using combined multi-scale 2D and 3D imaging. J. Volcanol. Geotherm. Res. 336, 179–191.
ISRM, 2007. The complete ISRM suggested methods for rock characterization, testing and monitoring: 1974–2006. In: Ulusay, R., Hudson, J.A. (Eds.), Suggested Methods Prepared by the Commission of Testing Methods, ISRM, Compilation Arranged by the ISRM Turkish International Group. Kozam Ofset, Ankara, Turkey.
Jaeger, J.C., Cook, N.G., Zimmerman, R., 2009. Fundamentals of Rock Mechanics, 4th ed. Wiley-Blackwell, p. 488.
Jamtveit, B., Kobchenko, M., Austrheim, H., Malthe-Sørenssen, A., Røyne, A., Svensen, H., 2011. Porosity evolution and crystallization-driven fragmentation during weathering of andesite. J. Geophys. Res. Solid Earth 116 (B12).
Jaupart, C., Allègre, C.J., 1991. Gas content, eruption rate and instabilities of eruption regime in silicic volcanoes. Earth Planet. Sci. Lett. 102 (3–4), 413–429.
Kennedy, B.M., Jellinek, A.M., Russell, J.K., Nichols, A.R.L., Vigouroux, N., 2010. Time- and temperature-dependent conduit wall porosity: a key control on degassing and explosivity at Tarawera volcano, New Zealand. Earth Planet. Sci. Lett. 299 (1–2), 126–137.
Landis, E.N., Keane, D.T., 2010. X-ray microtomography. Mater. Charact. 61, 1305–1316.
Larrea, P., França, Z., Widom, E., Lago, M., 2018. Petrology of the Azores Islands. In: Kueppers, U., Beier, C. (Eds.), Volcanoes of the Azores. Active Volcanoes of the World. Springer, Berlin, Heidelberg. https://doi.org/10.1007/978-3-642-32226-6_10.
Lavallée, Y., Kendrick, J.E., 2021. A Review of the Physical and Mechanical Properties of Volcanic Rocks and Magmas in the Brittle and Ductile Regimes. In: Forecasting and planning for volcanic hazards, risks, and disasters, pp. 153–238.
Le Bas, M.J., Le Maitre, R.W., Streckeisen, A., Zanettin, B., 1986. A Chemical Classification of Volcanic Rocks Based on the Total Alkali-Silica Diagram. J. Petro. 27, 745–750. https://doi.org/10.1093/petrology/27.3.745.
Le Maitre, R., Streckeisen, A., Zanettin, B., Le Bas, M., Bonin, B., Bateman, P., 2002. Igneous rocks: A classification and glossary of terms. In: Recommendations of the International Union of Geological Sciences Subcommission on the Systematics of Igneous Rocks, 2nd ed. Cambridge University Press. https://doi.org/10.1017/CBO9780511535581.
Lintao, Y., Marshall, A.M., Wanatowski, D., Stace, R., Ekneligoda, T., 2017. Effect of high temperatures on sandstone–a computed tomography scan study. Int. J. Phys. Model Geotech. 17 (2), 75–90.
Liu, C., Buono, G., Pappalardo, L., Shan, X., Yi, J., Shi, Y., Ventura, G., 2023. X-ray computed microtomography revealing the effects of volcanic, alteration, and burial processes on the pore structure of rocks from unconventional reservoirs (Songliao Basin, NE China). Geoenergy Sci. Eng 226, 211781. https://doi.org/10.1016/j.geoen.2023.211781.
Loaiza, S., Fortin, J., Schubnel, A., Gueguen, Y., Vinciguerra, S., Moreira, M., 2012. Mechanical behavior and localized failure modes in a porous basalt from the Azores. Geophys. Res. Lett. 39 (19).
Malheiro, A., 2006. Geological hazards in the Azores archipelago: Volcanic terrain instability and human vulnerability. J. Volcanol. Geotherm. Res. 156 (1–2), 158–171.
Malheiro, A., Nunes, J.C., 2007. In: Rocks, Volcanic, Malheiro & Nunes (Eds.), Volcanostratigraphic Profiles for the Azores Region: A Contribution for the EC8 Regulations and the Characterization of Volcanic Rocks Geomechanical Behaviour. Taylor & Francis Group, London, pp. 59–64.
Malheiro, A., Amaral, P., Vieira de Sousa, J.F., Miranda, V., 2018. Geomechanical characterization of volcanic rock materials from Azores and Madeira Archipelagos. 16° National Congress of Geotechnics (CNG), 27th to 30th May, Ponta Delgada, p. 12.
Małkowski, P., Ostrowski, Ł., Brodny, J., 2018. Analysis of Young's modulus for Carboniferous sedimentary rocks and its relationship with uniaxial compressive strength using different methods of modulus determination. J. Sustain. Min. 17 (3), 145–157.
McBeck, J.A., Cordonnier, B., Vinciguerra, S., Renard, F., 2019. Volumetric and shear strain localization in Mt. Etna basalt. Geophys. Res. Lett. 46 (5), 2425–2433.
McBeck, J., Ben-Zion, Y., Renard, F., 2020. The mixology of precursory strain partitioning approaching brittle failure in rocks. Geophys. J. Int. 221 (3), 1856–1872.
Miranda, J.M., Luis, J.F., Lourenço, N., RMS, Fernandes, 2015. The structure of the Azores Triple Junction: Implications for São Miguel Island. In: Gaspar, J.L., Guest, J. E., Duncan, A.M., FJAS, Barriga, Chester, D.K. (Eds.), Volcanic geology of São Miguel Island (Azores Archipelago), 44. Geological Society, London, Memoirs, pp. 5–13. https://doi.org/10.1144/M44.2.
Moore, R., 1991a. Geology of three late Quaternary stratovolcanoes on São Miguel, Azores. USGS Bull. 1900, 1–26.
Moore, R., 1991b. Geological map São Miguel. Azores. USGS Miscellaneous Investigations Series Map 1–2007.
Moreira, M., Wallenstein, N., 2012, April. Evolution of elastic properties and acoustic emission during uniaxial loading of rocks from the Fogo Volcano in the Island of São Miguel, Azores: Preliminary results. In: EGU General Assembly Conference Abstracts, p. 8830.
Muecke, G., Ade-Hall, J., Aumento, F., MacDonald, A., Reynolds, P., Hyndman, R., Quintina, J., Opdyke, N., Lowrie, W., 1974. Deep drilling in an active geothermal area in the Azores. Nature 252, 281–285. https://doi.org/10.1038/252281a0.
Nara, Y., Morimoto, K., Hiroyoshi, N., Yoneda, T., Kaneko, K., Benson, P.M., 2012. Influence of relative humidity on fracture toughness of rock: implications for subcritical crack growth. Int. J. Solids Struct. 49 (18), 2471–2481.

Noiriel, C., Renard, F., 2022. Four-dimensional X-ray micro-tomography imaging of dynamic processes in geosciences. Compt. Rendus Géosci. 354 (G2), 255–280.
Ohta, T., Arai, H., 2007. Statistical Empirical Index of Chemical Weathering in Igneous Rocks: A New Tool for Evaluating the Degree of Weathering. Chem. Geol. 240, 280–297. https://doi.org/10.1016/j.chemgeo.2007.02.017.
Okada, J., Sigmundsson, F., Ófeigsson, B.G., Ferreira, T., Rodrigues, R.M.M.T.C., 2015. Tectonic and volcanic deformation at São Miguel Island, Azores, observed by continuous GPS analysis 2008-2013. In: Gaspar, J.L., Guest, J.E., Duncan, A.M., Barriga, F.J.A.S., Chester, D.K. (Eds.), Volcanic Geology of São Miguel Island (Azores Archipelago), vol. 44. Geological Society, London, Memoirs, pp. 239–256. https://doi.org/10.1144/M44.18.
Pappalardo, G., Mineo, S., 2017. Investigation on the mechanical attitude of basaltic rocks from Mount Etna through InfraRed Thermography and laboratory tests. Constr. Build. Mater. 134, 228–235.
Pappalardo, G., Punturo, R., Mineo, S., Contrafatto, L., 2017. The role of porosity on the engineering geological properties of 1669 lavas from Mount Etna. Eng. Geol. 221, 16–28.
Pappalardo, L., Buono, G., Fanara, S., Petrosino, P., 2018. Combining textural and geochemical investigations to explore the dynamics of magma ascent during Plinian eruptions: a Somma–Vesuvius volcano (Italy) case study. Contrib. Mineral. Petrol. 173, 61. https://doi.org/10.1007/s00410-018-1486-x.
Pappalardo, L., Buono, G., Procesi, M., Etiope, G., 2024. The link between ophiolitic chromitites, natural hydrogen and methane: Insights from 3D microtomography. Chem. Geol. 122575. https://doi.org/10.1016/j.chemgeo.2024.122575.
Pereira, M.L., Matias, D., Viveiros, F., Moreno, L., Silva, C., Zanon, V., Uchôa, J., 2022. The contribution of hydrothermal mineral alteration analysis and gas geothermometry for understanding high-temperature geothermal fields–the case of Ribeira Grande geothermal field. Azores. Geotherm. 105, 102519. https://doi.org/10.1016/j.geothermics.2022.102519.
Pereira, M.L., Pappalardo, L., Buono, G., Zanon, V., Fernandes, I., 2023a. Microstructural, textural, and physical characteristics of volcanic rocks from Fogo volcano – S. Miguel Island (Azores), Portugal. Paper presented at MedGU 2023, 26-30 November, Istanbul, p. 5.
Pereira, M.L., Dionísio, A., Garcia, M.B., Bento, L., Amaral, P., Ramos, M., 2023b. Natural stone heterogeneities and discontinuities: an overview and proposal of a classification system. Bull. Eng. Geol. Environ. 82, 152. https://doi.org/10.1007/s10064-023-03152-0.
Pereira, M.L., Zanon, V., Fernandes, I., Pappalardo, L., Viveiros, F., 2024. Hydrothermal alteration and physical and mechanical properties of rocks in a volcanic environment: a review. Earth Sci. Rev. 104754.
PerGeos, 2021. The Digital Rock Analysis Software – PerGeos User's Guide. Thermo Fisher Scientific. http://www.thermofisher.com/pergeos.
Polacci, M., Arzilli, F., La Spina, G., Le Gall, N., Cai, B., Hartley, M.E., Di Genova, D., Vo, N.T., Nonni, S., Atwood, R.C., Llewellin, E.W., Lee, P.D., Burton, M.R., 2018. Crystallisation in basaltic magmas revealed via in situ 4D synchrotron X-ray microtomography. Sci. Rep. 8 (1), 8377.
Qajar, J., Arns, C.H., 2022. Chemically induced evolution of morphological and connectivity characteristics of pore space of complex carbonate rock via digital core analysis. Water Resoue. Res. 58 (3), e2021WR031298. https://doi.org/10.1029/2021WR031298.
Queiroz, G., Gaspar, J.L., Guest, J.E., Gomes, A., Almeida, M.H., 2015. Eruptive history and evolution of Sete Cidades Volcano, São Miguel Island, Azores. In: Gaspar, J.L., Guest, J.E., Duncan, A.M., Barriga, F.J.A.S., Chester, D.K. (Eds.), Volcanic Geology of São Miguel Island (Azores Archipelago), vol. 44. Geological Society, London, Memoirs, pp. 87–104. https://doi.org/10.1144/m44.7.
Reinoso, J., Durand, P., Budarapu, P.R., Paggi, M., 2019. Crack patterns in Heterogenous Rocks using a combined phase Field-Cohesive Interface Modeling Approach: a Numerical Study. Energies 12 (6), 965. https://doi.org/10.3390/en12060965.
Rose, D.A., 1963. Water movement in porous materials: Part 2-The separation of the components of water movement. Br. J. Appl. Phys. 14 (8), 491.
Rust, A.C., Cashman, K.V., 2011. Permeability controls on expansion and size distributions of pyroclasts. J. Geophys. Res. Solid Earth 116 (B11).
Schepp, L.L., Ahrens, B., Balcewicz, M., et al., 2020. Digital rock physics and laboratory considerations on a high-porosity volcanic rock. Sci. Rep. 10, 5840. https://doi.org/10.1038/s41598-020-62741-1.
Searle, R., 1980. Tectonic pattern of the Azores spreading Centre and triple junction. Earth Planet. Sci. Lett. 51 (2), 415–434.
Shea, T., Houghton, B.F., Gurioli, L., Cashman, K.V., Hammer, J.E., Hobden, B.J., 2010. Textural studies of vesicles in volcanic rocks: an integrated methodology. J. Volcanol. Geotherm. Res. 190, 271–289.
Silva, R., Ferreira, T., Gaspar, J.L., 2015. Seismic activity on São Miguel Island volcano-tectonic structures (Azores archipelago). In: Gaspar, J.L., Guest, J.E., Duncan, A.M., Barriga, F.J.A.S., Chester, D.K. (Eds.), Volcanic Geology of São Miguel Island (Azores Archipelago), vol. 44. Geological Society, London, Memoirs, pp. 227–237. https://doi.org/10.1144/M44.17.
Song, S.R., Jones, K.W., Lindquist, B.W., Dowd, B.A., Sahagian, D.L., 2001. Synchrotron X-ray computed microtomography: Studies on vesiculated basaltic rocks. Bull. Volcanol. 63, 252–263.
Sparks, R.S.J., Annen, C., Blundy, J.D., Cashman, K.V., Rust, A.C., Jackson, M.D., 2019. Formation and dynamics of magma reservoirs. Philos Trans R Soc A 377 (2139), 20180019.
Streckeisen, A., 1978. IUGS Subcommission on the Systematics of Igneous Rocks. Classification and nomenclature of volcanic rocks, lamprophyres, carbonatites and melilitic rocks: Recommendations and suggestions. Neues Jahrb. Mineral., Abh. 134, 1–14.
Tang, C.A., Liu, H., Lee, P.K.K., Tsui, Y., Tham, L., 2000. Numerical studies of the influence of microstructure on rock failure in uniaxial compression—part I: effect of heterogeneity. Int. J. Rock Mech. Min. Sci. 37 (4), 555–569.
Tang, C.A., Tham, L.G., Wang, S.H., Liu, H., Li, W.H., 2007. A numerical study of the influence of heterogeneity on the strength characterization of rock under uniaxial tension. Mech. Mater. 39 (4), 326–339.
Török, Á., Přikryl, R., 2010. Current methods and future trends in testing, durability analyses and provenance studies of natural stones used in historical monuments. Eng. Geol. 115 (3–4), 139–142.
Trota, A., 2009. Crustal deformation studies in S. Miguel and Terceira Islands (Azores). Volcanic unrest evaluation in Fogo/Congro area (S. Miguel). PhD Thesis in Geology. Universidade dos Açores, p. 281.
Turk, N., Dearman, W.R., 1986. A correction equation on the influence of length-to-diameter ratio on the uniaxial compressive strength of rocks. Eng. Geol. 22 (3), 293–300.
Vairé, E., Heap, M.J., Baud, P., van Wyk de Vries, B., 2024. Quantifying the physical and mechanical heterogeneity of porous volcanic rocks from the Chaîne des Puys (Massif Central, France). Bull. Volcanol. 86 (5), 49.
Van Stappen, J.F., De Kock, T., De Schutter, G., Cnudde, V., 2019. Uniaxial compressive strength measurements of limestone plugs and cores: a size comparison and X-ray CT study. Bull. Eng. Geol. Environ. 78, 5301–5310. https://doi.org/10.1007/s10064-018-01448-0.
Vieira, L.D., Moreira, A.C., Mantovani, I.F., Honorato, A.R., Prado, O.F., Becker, M., Fernandes, C.P., Waichel, B.L., 2021. The influence of secondary processes on the porosity of volcanic rocks: a multiscale analysis using 3D X-ray microtomography. Appl. Radiat. Isot. 172, 109657.
Villeneuve, M.C., Diederichs, M.S., Kaiser, P.K., 2012. Effects of grain scale heterogeneity on rock strength and the chipping process. Int. J. Geomech. 12 (6), 632–644.
Walker, G.P.L., 1987. Pipe vesicles in Hawaiian basaltic lavas: their origin and potential as paleoslope indicators. Geology 15, 84–87. https://doi.org/10.1130/0091-7613(1987)15<84:PVIHBL>2.0.CO;2.
Wallenstein, N., Duncan, A., Guest, J.E., Almeida, M.H., 2015. Eruptive history of Fogo Volcano, São Miguel, Azores. In: Gaspar, J.L., Guest, J.E., Duncan, A.M., Barriga, F.J.A.S., Chester, D.K. (Eds.), Volcanic Geology of São Miguel Island (Azores Archipelago), vol. 44. Geological Society, London, Memoirs, pp. 105–123. https://doi.org/10.1144/M44.8.
Winkler, E.M., 1997. Stone in Architecture: Properties, Durability. Springer, Berlin, Heidelberg, New York.
Xu, T., Fu, T.F., Heap, M.J., Meredith, P.G., Mitchell, T.M., Baud, P., 2020. Mesoscopic damage and fracturing of heterogeneous brittle rocks based on three-dimensional polycrystalline discrete element method. Rock Mech. Rock. Eng. 53 (12), 5389–5409.
Yoshinaka, R., Osada, M., Park, H., Sasaki, T., Sasaki, K., 2008. Practical determination of mechanical design parameters of intact rock considering scale effect. Eng. Geol. 96 (3–4), 173–186. https://doi.org/10.1016/j.enggeo.2007.10.008.
Zanon, V., 2015. The magmatism of the Azores islands. In: Gaspar, J.L., Guest, J.E., Duncan, A.M., Barriga, F.J.A.S., Chester, D.K. (Eds.), Volcanic Geology of São Miguel Island (Azores Archipelago), vol. 44. Geological Society, London, Memoirs, pp. 51–64. https://doi.org/10.1144/M44.5.
Zhang, S., Shen, Q., 2023. Effects of Pore–Crack Relative Location on Crack Propagation in Porous Granite Based on the Phase-Field Regularized Cohesion Model. Materials 16 (23), 7474. https://doi.org/10.3390/ma16237474.
Zhu, W., Baud, P., Vinciguerra, S., Wong, T.-f., 2016. Micromechanics of brittle faulting and cataclastic flow in Mount Etna basalt. J. Geophys. Res. Solid Earth 121, 4268–4289. https://doi.org/10.1002/2016JB012826.
Zorn, E.U., Rowe, M.C., Cronin, S.J., Ryan, A.G., Kennedy, L.A., Russell, J.K., 2018. Influence of porosity and groundmass crystallinity on dome rock strength: a case study from Mt. Taranaki, New Zealand. Bull. Volcanol. 80, 1–17.
Zou, C., 2013. Volcanic Reservoirs in Petroleum Exploration, first ed. Elsevier, Petroleum Industry Press, China, p. 204.